Nature Communications

https://doi.org/10.1038/s41467-026-71326-x

Article in Press

FRZB-induced anti-angiogenic effect via Caveolin-1-mediated TGFβ signalling

Received: 1 September 2025

Accepted: 17 March 2026

Cite this article as: Chen, C.-J., Zhou, L., Chen, H.-T. *et al.* FRZB-induced anti-angiogenic effect via Caveolin-1-mediated TGFβ signalling. *Nat Commun* (2026). https://doi.org/10.1038/s41467-026-71326-x

Ching-Jou Chen, Lei Zhou, Han-Tang Chen, Veluchamy Amutha Barathi, Beiying Qiu, Asfa Alli-Shaik, Rui Ning Chia, Seok Ting Lim, Chaemin Joo, Ning Cheung, Choi Mun Chan, Siew Kwan Koh, Alison Tan, Ravi Kumar Verma, Hao Fan, Weihua Song, David Virshup, Jayantha Gunaratne, Tien Yin Wong, Gemmy Chui Ming Cheung, Wanjin Hong & Xiaomeng Wang

Title: FRZB-induced anti-angiogenic effect via Caveolin-1-mediated TGFβ singalling

Author list: Ching-Jou Chen [1]*, Lei Zhou [2,3]*, Han-Tang Chen [1,4], Veluchamy Amutha Barathi [1,4,5], Beiying Qiu [1,4], Asfa Alli-Shaik [6], Rui Ning Chia [1,4], Seok Ting Lim [1,4], Chaemin Joo [1,4], Ning Cheung [1,7], Choi Mun Chan [7], Siew Kwan Koh [4], Alison Tan [1,4], Ravi Kumar Verma [8], Hao Fan [8,9], Weihua Song (宋伟华) [1], David Virshup [1], Jayantha Gunaratne [6,10], Tien Yin Wong [1,7,11], Gemmy Cheung Chui Ming [1,4,7], Wanjin Hong [6], Xiaomeng Wang [1,4,6]§

Affiliations:

[1] Duke-NUS Medical School, 8 College Road, Singapore

[2] School of Optometry, Department of Applied Biology and Chemical Technology, Research Centre for SHARP Vision (RCSV), The Hong Kong Polytechnic University, Hong Kong

[3] Centre for Eye and Vision Research (CEVR), 17W Hong Kong Science Park, Hong Kong

[4] Singapore Eye Research Institute, The Academia, 20 College Road, Singapore

[5] Department of Ophthalmology, Yong Loo Lin School of Medicine, National University of Singapore

[6] Institute of Molecular and Cell Biology (IMCB), Agency for Science, Technology and Research (A*STAR), 61 Biopolis Drive, Proteos, Singapore 138673, Singapore

[7] Singapore National Eye Centre, 11 Third Hospital Ave, Singapore

[8] Bioinformatics Institute, Agency for Science, Technology and Research, 30 Biopolis Street, Singapore

[9] Institute for Molecular and Cellular Therapeutics, Chinese Institutes for Medical Research, Beijing, China

[10] Yong Loo Lin School of Medicine, National University of Singapore, Singapore

[11] Beijing Visual Science and Translational Eye Research Institute (BERI), Tsinghua Medicine, Medical Sciences Building, Tsinghua University, Beijing, China

* These authors contributed equally to this work

§ Corresponding author: xiaomeng.wang@duke-nus.edu.sg

Abstract

Pathological neovascularization and vascular leakage are central drivers of many sight-threatening diseases. While strategies targeting vascular endothelial growth factor (VEGF) have improved clinical outcomes, many patients do not benefit from the treatment, highlighting the need for alternative therapeutic strategies. Two independent vitreous proteomics studies in patients with proliferative diabetic retinopathy (PDR) reveal a significant reduction in Frizzled-related Protein (FRZB), a finding recapitulated in preclinical models of ocular angiogenesis. Here, we show that loss of *Frzb* exacerbates ocular angiogenesis, whereas therapeutic delivery of Fc-recombinant FRZB or its netrin-related motif (NTR) robustly suppresses and reverses ocular angiogenesis across various preclinical models. Fc-NTR acts additively with Aflibercept, supporting its potential as a combination therapy. Mechanistically, FRZB binds Caveolin-1 (CAV1), inhibits its phosphorylation at Tyr42, promotes retention of the TGFβ receptor ALK5, and enhances Smad2/3 signalling. These findings define FRZB as a potent suppressor of ocular angiogenesis and establish a promising therapeutic avenue.

Introduction

Abnormal angiogenesis and vascular remodelling are critical contributors to many pathological conditions, including cancers, cardiovascular disorders, and blinding eye diseases such as neovascular age-related macular degeneration (nAMD) and proliferative diabetic retinopathy (PDR) [1]. These conditions affect tens of millions worldwide and impose a significant socioeconomic burden [2,3]. Current treatment strategies and investigative drugs primarily focus on inhibiting vascular endothelial growth factor (VEGF), which has shown clinical success in controlling neovascularization and vascular leakage [4]. However, a significant proportion of patients either fail to respond or develop resistance to anti-VEGF therapy over time [5,6]. This limitation is often attributed to the activation of alternative angiogenic pathways that bypass VEGF inhibition [7]. Addressing these pathways could thus offer innovative strategies to control disease progression and improve visual outcomes, particularly in patients with suboptimal responses to current anti-VEGF agents.

Among the alternative pathways implicated in angiogenesis, Wnt signalling plays a pivotal role in neovascularization and vascular remodelling [8]. Loss-of-function mutations in key components of this pathway, such as FZD4, LRP5, and Norrin, lead to profound vascular defects in the eye [9,10].

Pharmacological modulation of Wnt signalling has shown therapeutic promise. For example, a bifunctional antibody targeting LRP5 and FZD4 (Restoret) reduces vascular leakage in clinical trials for several ocular angiogenic diseases, including nAMD and DME [11,12]. Additionally, small-molecule inhibitors targeting various components of the Wnt signalling pathway are being explored in oncology for their anti-angiogenic effects [13]. The Wnt signalling pathway is evolutionarily conserved and plays a crucial role in both development and disease. Its activity is tightly regulated by diverse modulators to ensure precise spatial and temporal control. Among these modulators, secreted frizzled-related proteins (sFRPs) act as key extracellular regulators. sFRPs consist of a signalling peptide, an N-terminal Cysteine-Rich Domain (CRD) which shares sequence homology with the ligand-binding domain of Frizzled transmembrane Wnt receptors, and a Netrin-like C-terminal domain NTR [14]. Depending on the context, sFRPs can exert either positive or negative effects on Wnt signalling [14-18]. Moreover, Wnt-independent roles for sFRPs have also been reported in various pathological processes [19]. Despite these findings, the roles of sFRPs in pathological angiogenesis, particularly in the eye, and the function of their distinct domains, remain poorly understood.

In this study, we systematically investigated alternative pathways and molecular mechanisms underlying ocular angiogenesis and vascular remodelling, aiming to identify novel therapeutic targets for vision-threatening retinal diseases. Using two independent vitreous proteomics analyses, we identified a significant reduction in frizzled-related protein (FRZB) levels in patients with PDR. Consistent with this finding, *Frzb* expression was markedly downregulated in ocular tissues at the peak of pathological neovascularization in two mouse models: laser-induced choroidal neovascularization (CNV) and oxygen-induced retinopathy (OIR). Functional studies revealed that loss of *Frzb* in mice exacerbated ocular angiogenesis, whereas treatment with Fc

recombinant protein containing full-length FRZB (Fc-FRZB) or its C-terminal fragment NTR (Fc-NTR), but not the CRD (Fc-CRD), potently suppressed endothelial cell activation and angiogenesis across multiple *in vitro*, *ex vivo*, and *in vivo* models. Importantly, Fc-FRZB and Fc-NTR not only prevented but also reversed established ocular neovascularization in several preclinical models, highlighting their therapeutic potential. Furthermore, Fc-NTR demonstrated synergistic efficacy when combined with the anti-VEGF agent Aflibercept, supporting its utility as a complementary strategy to enhance the treatment efficacy of the current standard of care.

Mechanistically, FRZB exerts its anti-angiogenic effects independently of Wnt signalling. It binds directly to Caveolin-1 (CAV-1), a membrane scaffolding protein, inhibits its phosphorylation at a previously unreported Tyrosine 42 (Tyr42) site, and subsequently increases the levels of the anti-angiogenic Transforming growth factor (TGF)β type I receptor ALK5 in retinal microvascular endothelial cells (HREC). This leads to the cytoplasmic accumulation of phosphorylated Smad2/3, a key downstream signalling transducer of TGFβ. Notably, HRECs expressing a constitutively active form of CAV-1 (Y42D) were refractory to the inhibitory effects of FRZB on angiogenesis, confirming a central role for this FRZB-CAV-1-TGFβ signalling axis.

In summary, our findings uncovered a previously unrecognised mechanism of angiogenic regulation and established the NTR domain of FRZB as a promising therapeutic strategy to address the limitations of current VEGF-targeted therapies. Beyond the eye, this strategy may also hold therapeutic potential for systemic angiogenic diseases.

Results

FRZB is Significantly Reduced in Angiogenic Eyes

We previously reported label-based tandem mass tag (TMT)-based quantitative proteomics analysis of vitreous samples from patients with PDR, using epiretinal membrane (ERM) patient samples as controls [20]. Among ~1200 proteins quantified across both sample types, FRZB was significantly downregulated in the vitreous of PDR patients (Fig. 1A). This observation was further validated in an independent patient cohort by comparing vitreous samples from PDR patients and non-PDR patients with retinal detachment (RD), using a label-free data-independent acquisition-based SWATH-MS analysis (Fig. 1B), and confirmed by western blot analysis (Fig. 1C). Next, we investigated whether the *Frzb* transcript is reduced in ocular tissues during pathological neovascularization using two well-established mouse models. The oxygen-induced retinopathy (OIR) model mimics hypoxia-driven retinal neovascularization in PDR [21]. Consistent with the data obtained in human patients, *Frzb* mRNA and protein levels were significantly reduced in P17 OIR retinae, corresponding to the peak of pathological neovascularization (Fig. 1D, Supplementary Fig. 1A). In another model, choroidal neovascularization (CNV) was induced by laser [22]. Similarly, *Frzb* transcript and protein levels were lower in the retinal pigment epithelium (RPE)/choroidal complex 14 days after laser, coinciding with the peak of CNV formation (Fig. 1E, Supplementary Fig. 1B). These findings suggest that *Frzb* downregulation is a conserved feature of both retinal and choroidal neovascularization across different species.

To further elucidate the role of FRZB in ocular angiogenesis, we evaluated its expression across different compartments of the mouse eye. Our findings revealed that *Frzb* mRNA is expressed at significantly higher levels in the neuroretina compared to the RPE/choroid complex (Fig. 1F). RNAscope analysis further demonstrated that *Frzb* transcripts are highly enriched in Müller cells within the inner nuclear layer (INL), as evidenced by co-localization with the Müller cell marker Glutamine Synthetase (GS) (Fig. 1G). This expression pattern was corroborated by qRT-PCR

analysis of various human ocular cell lines, which showed high *Frzb* expression in Müller cells (Fig. 1H). Collectively, these results indicate that *Frzb* is constitutively expressed in Müller cells of the neuroretina and its expression is decreased during pathological neovascularization, underscoring its potential role in ocular vascular remodelling.

Functional Consequences of *Frzb* Deletion in Ocular Neovascularization

To examine the impact of *Frzb* loss on retinal vascular development, we first analysed developmental retinal angiogenesis in *Frzb* knockout (*Frzb*$^{-/-}$) mice. In contrast to other Wnt pathway regulators, such as FZD4, Lrp5, and Norrin, where loss of function leads to severe vascular defects [23-25], *Frzb*$^{-/-}$ mice were viable and displayed no gross developmental abnormalities. However, *Frzb* deficiency did affect the kinetics of vessel growth. At postnatal day 4 (P4), *Frzb*$^{-/-}$ retinae exhibited a significant increase in radial expansion and capillary density of the superficial vascular plexus compared to wild-type littermates (Fig. 2A). The elevation in capillary density in *Frzb*$^{-/-}$ retinae continued until P10 (Fig. 2B), which gradually resolved afterwards (Supplementary Fig. 2A). These findings suggest that FRZB acts as a transient negative regulator of early postnatal retinal angiogenesis.

Given the observed reduction in *Frzb* transcript and protein levels in the retina and RPE/choroid complex of C57BL/6 mice subjected to OIR and laser-induced CNV, respectively, we next investigated the impact of *Frzb* deletion on pathological ocular angiogenesis. In the OIR model, where retinal neovascularization peaks at P17 [21], *Frzb*$^{-/-}$ mice exhibited significantly exacerbated neovascular tufts, whereas the avascularisation area remain unchanged, compared to littermate controls (Fig. 2C). Similarly, in the laser-induced CNV model, fundus fluorescein angiography (FFA) performed at day 14 post-laser injury revealed a significant increase in vascular leakage and lesion size in *Frzb*$^{-/-}$ mice (Fig. 2D). These findings were corroborated by RPE flatmounts stained

for the vascular marker CD31, which demonstrated approximately a twofold increase in both lesion area (Fig. 2E) and lesion volume (Supplementary Fig. 2B) in the absence of *Frzb*. Intriguingly, transcript levels of key angiogenic factors, including *Vegf* and *Fgf2*, as well as components of the Wnt signalling pathway (*Fzd4*, *Lrp5*, and *Axin2*), remained unchanged in retinae of *Frzb*$^{-/-}$ mice at the peak of developmental angiogenesis (Supplementary Fig. 3A - E) and OIR (Supplementary Fig. 4A - E), and in the choroid/RPE complex during CNV (Supplementary Fig. 5A - E). Conversely, the expression of mediators involved in vascular remodelling, including *Angpt1*, *Angpt2*, and *Pdgfb*, was reduced to varying extent in the eyes of *Frzb*$^{-/-}$ mice during developmental and pathological angiogenesis (Supplementary Fig. 3F – H, Supplementary Fig. 4F – H, and Supplementary Fig. 5F – H). These findings collectively revealed a critical role of *Frzb* in ocular angiogenesis and vascular remodelling, particularly under pathological conditions, possibly *via* a VEGF, FGF2, and Wnt-independent mechanism.

FRZB and Its NTR Domain Inhibit Endothelial Cell Activation and Angiogenesis *in vitro* and *ex vivo*

FRZB is a highly conserved member of the sFRP family of proteins (Supplementary Fig. 6), suggesting that it may serve a critical functional role. Like other sFRPs, FRZB contains two distinct functional domains (Supplementary Fig. 7). The cysteine-rich domain (CRD) at the N terminus shares sequence homology with the CRD of Frizzled and is therefore thought to compete with Frizzled for binding to Wnt ligands[26]. The netrin-related motif (NTR) at the C-terminus is homologous to tissue inhibitors of metalloproteases (TIMPs), although its precise function remains to be elucidated.

To investigate the role of FRZB in angiogenesis and identify its functional domains, we generated Fc-fusion proteins (Supplementary Fig. 8A and B) encoding either full-length FRZB (Fc-FRZB), its CRD domain (Fc-CRD), or its NTR domain (Fc-NTR).

Endothelial cells respond to angiogenic cues by transitioning to a proliferative and migratory phenotype, enabling the formation of tube-like structures [27]. To investigate the functional roles of FRZB, we used human retinal microvascular endothelial cell (HREC)-based *in vitro* models and multiple *ex vivo* models of angiogenesis. We showed that Fc-FRZB and Fc-NTR, but not Fc-CRD, markedly inhibited HREC proliferation (Fig. 3A). Similarly, Fc-FRZB and Fc-NTR reduced total tube length and the number of junctions formed by HREC in growth factor-reduced Matrigel ® (Fig. 3B) and impaired HREC migration across the Transwell (Fig. 3C). Interaction between leukocytes and ECs results in increased vascular permeability and altered endothelial responsiveness to microenvironmental cues, which are frequently associated with pathological angiogenesis [28]. Fc-FRZB and Fc-NTR effectively inhibited TNFα-induced monocyte adhesion to HRECs (Fig. 3D). Furthermore, Fc-FRZB and Fc-NTR displayed potent inhibitory effects on vessel outgrowth from choroid (Fig. 3E), aortic ring (Fig. 3F), and metatarsal (Fig. 3G) explants. Together, these findings provide compelling evidence for the anti-angiogenic activity of FRZB and identify the NTR domain as the key mediator of its effect.

FRZB and NTR Prevent and Reverse Ocular Angiogenesis *in vivo*

To further evaluate the therapeutic potential of FRZB-based therapeutic molecules, we tested the *in vivo* efficacy of Fc-FRZB and Fc-NTR, administered either as monotherapies or in combination with the current standard of care, Aflibercept, in the laser-induced CNV model. Fc-FRZB or Fc-NTR, with or without Aflibercept, was delivered *via* intravitreal injection immediately after laser treatment in C57BL/6 mice (Fig. 4A). At day 14 post-laser, FFA revealed a superior anti-

angiogenic efficacy of Fc-NTR relative to an equivalent dose of Aflibercept, whereas Fc-FRZB demonstrated non-inferior efficacy (Fig. 4B). Moreover, combination treatment with either Fc-FRZB or Fc-NTR and Aflibercept resulted in further suppression of CNV lesion size compared with Aflibercept monotherapy (Fig. 4B). RPE flatmount stained for the endothelial marker CD31 demonstrated a potent anti-angiogenic efficacy of Fc-FRZB and Fc-NTR either as a monotherapy or in combination with Aflibercept (Fig. 4C).

Having established the preventive efficacy, we next evaluated the ability of these agents to regress the established CNV. Intravitreal injections were performed seven days post-laser injury, when CNV lesions were already established (Fig. 4D). Both Fc-FRZB and Fc-NTR significantly induced regression of CNV lesions, again with efficacy comparable to Aflibercept (Fig. 4E and F). To assess the therapeutic efficacy of systemically delivered Fc-NTR on retinal neovascularization, C57BL/6 mice were administered Fc-NTR (25mg/kg) *via* intraperitoneal injection at P12, following a 5-day exposure to 75% oxygen in a hypoxic chamber. Fc-NTR robustly suppressed pathological retinal neovascular tuft formation (Fig. 4G) without impairing physiological angiogenesis (Supplementary Fig. 9), demonstrating efficacy comparable to an equivalent dose of Aflibercept. Finally, the efficacy of Fc-NTR was assessed in a rabbit model of persistent retinal neovascularization (PRNV)[29], where a single intravitreal dose achieved sustained inhibition of both angiogenesis and vascular leakage for at least six weeks (Fig. 4H). Together, these data established FRZB-based therapeutic molecules, particularly Fc-NTR, as promising therapeutic candidates for both prevention and treatment of pathological ocular angiogenesis and leakage, with potential utility as monotherapies or in combination with existing anti-VEGF agents.

FRZB Controls Ocular Angiogenesis *via* Cav-1–Mediated TGFβ Receptor Dynamics

sFRPs are traditionally considered endogenous regulators of Wnt signalling due to the presence of CRD [14]. Indeed, FRZB has been shown to form a complex with multiple Wnt ligands and regulate their diffusion and signalling during *Xenopus* embryo development [30-35]. Among angiogenic Wnt ligands, Wnt 1 [36 37] and Wnt7a [38-45] are the two best-characterised. Notably, HRECs responded to Wnt1 but not Wnt 7a, and the treatment with Fc-NTR, the anti-angiogenic domain of FRZB, had no effect on either basal or Wnt1-induced phosphorylation of LRP6 and β-Catenin (Fig. 5A and Supplementary Fig. 10). These findings further support the notion that FRZB signals through a Wnt-independent pathway in ECs. Besides Wnt, sFRPs have been reported to regulate other angiogenic pathways, such as VEGF [46,47]. However, unlike Aflibercept, FRZB had no impact on VEGF-induced phosphorylation of VEGF receptor 2 in HRECs (Fig. 5B). Instead, FRZB increased the levels of the anti-angiogenic Transforming growth factor (TGF)β type I receptor ALK5 and its downstream signalling transducer phosphorylated Smad3, while the levels of the pro-angiogenic ALK1 receptor and phosphorylated Smad1/5 remained unchanged in HRECs (Fig. 5C). To confirm that the anti-angiogenic effect of FRZB is mediated through the ALK5-Smad3 pathway, we inhibited the activity of ALK5 with the small molecule inhibitor SB43152. This resulted in a complete loss of FRZB-induced Smad3 phosphorylation (Fig. 5D).

To further elucidate the molecular mechanism underlying FRZB-mediated anti-angiogenic effects, we performed a phospho-proteomics study on FRZB-treated HRECs. A total of 42 phospho-peptides, corresponding to 38 proteins, were differentially phosphorylated following Fc-FRZB treatment. Among these, phosphorylation of Caveolin-1 (CAV-1) at a previously unreported tyrosine 42 (Tyr42) site (localization probability = 1.000) showed the most significantly reduction in Fc-FRZB-treated HRECs (Fig. 5E and Supplementary Fig. 11A). Enriched ontology cluster analysis indicated that CAV-1 is an important hub protein in the network (Supplementary Fig.

11B). CAV-1 is a small, oligomeric scaffolding protein involved in generating membrane curvature, such as caveolae [48]. To investigate the role of CAV-1 Tyr42 phosphorylation in FRZB-regulated anti-angiogenic effects, HRECs were transfected with constitutively active CAV-1 constructs by replacing the classical Tyr14 or previously unreported Tyr42 with aspartic acid, respectively. Intriguingly, HRECs overexpressing CAV-1 Y42D but not CAV-1 Y14D were resistant to the inhibitory effect of FRZB on HREC tube formation (Fig. 5F). A similar resistance to the inhibitory effect of FRZB was observed in the Transwell migration assay using CAV-1 Y42D overexpressing HRECs (Fig. 5G). In addition, the FRZB-induced activation of ALK5-Smad3 signalling is also compromised in CAV-1 Y42D-overexpressing HRECs (Fig. 5H). Using a co-immunoprecipitation assay, we demonstrated a specific interaction between FRZB and CAV-1 in conditioned media, but not in HREC lysate (Fig. 5I), suggesting that this interaction likely occurs in the extracellular environment. While CAV-1 is classically known as an integral component of caveolae on the plasma membrane, it can also be secreted by various types of cells [49-53], including endothelial cells [54], *via* exosome-like vesicles to exert paracrine function.

To further support the direct interaction between FRZB and CAV1, we employed structural analysis of the HADDOCK3-generated complexes, which established the key interactions between the N-terminal region of CAV1 and the C-terminal NTR domain of FRZB (Fig. 5J). In the wild-type complex, a tyrosine residue at position 42 (Tyr42) plays a critical role at the protein-protein interface by directly interacting with the β-sheets within the NTR domain and contributing to complex stability. The extended aromatic side chain of Tyr42 facilitates the formation of hydrogen bonding with the backbone of β-sheets residues within the NTR domain of FRZB, thereby stabilizing the interprotein interface. Substitution of Tyr42 with aspartic acid (Y42D) disrupts this key interaction, resulting in the loss of favourable interfacial contacts. To evaluate the impact of

this mutation on complex formation, binding free energy calculations were performed (Table 1). The FRZB-CAV1 wild-type complex exhibited significantly more favourable binding energy (-104.2 ± 29.7 kcal/mol) compared to the FRZB-CAV1^{Y42D} mutant (-89.5 ± 28.1 kcal/mol). This corresponds to a positive ΔΔG of 14.7 kcal/mol, indicating a reduced binding affinity upon mutation, consistent with the observed disruption of interfacial interactions. In contrast, Tyr14 lies near the loop region within the NTR domain of FRZB in FRZB-CAV1 wild-type complex and does not form any specific contacts with FRZB. Our binding free energy calculations revealed that substituting Tyr14 with aspartic acid (Y14D) in CAV1 yields a ΔΔG of 7.5 kcal/mol, compared to 14.7 kcal/mol for the FRZB-CAV1^{Y42D} mutant. This smaller destabilization suggests that CAV1^{Y14D} does not disrupt the interfacial interactions with FRZB to the same extent as observed in the CAV1^{Y42D} mutant, potentially preserving the complex stability.

Discussion

Our study identifies FRZB as a potent and selective inhibitor of pathological neovascularization and vascular leakage in the eye. We show that this effect is mediated by its C-terminal NTR domain, rather than the Frizzled-related CRD, indicating a Wnt-independent mechanism of action. Mechanistically, FRZB engages a previously unrecognised signalling axis by binding to secreted CAV-1 and inhibiting its phosphorylation at a previously unreported Tyr42 site. As a consequence, it leads to stabilization of the anti-angiogenic TGFβ type I receptor ALK5 and accumulation of its downstream signalling mediator pSmad3. This FRZB-CAV-1-TGFβ pathway provides exciting insights into sFRP signalling, traditionally viewed as a Wnt ligand-binding modulator.

Previous studies have linked FRZB to the Wnt pathway through interacting with Wnt1, Wnt7, and Wnt8 and regulating their diffusion and signalling during Xenopus embryo development [31,32,34,35]. While Wnt1 [37,55], and Wnt7[38,41,45] have been associated with angiogenesis in non-ocular tissues, our data show that only Wnt1 activates LRP6-β-catenin signalling in HRECs, and FRZB doesn't affect either basal or Wnt1-induced canonical Wnt signalling in this context. This aligns with the finding that the Wnt-binding CRD is dispensable for the anti-angiogenic activity of FRZB in the eye. Such findings are consistent with the broader functional diversity of sFRP family proteins, which extend beyond Wnt ligand regulation to interactions with Frizzled [19] and fibronectin-integrin complexes [56], BMP[16,57-60], and other signalling molecules. It is worth noting that the NTR of FRZB shares a low sequence homology with the NTR of other sFRP family proteins (Supplementary Fig. 12A and B) but is highly similar to Netrin-1, a pro-angiogenic neural guidance cue [61,62], which may underlie its unique functional role compared to other sFRPs. CD146 was previously identified as a receptor for Netrin-1; however, its interaction involved the domain V, instead of the NTR domain of Netrin-1 [63].

Our phosphor-proteomics analysis revealed that FRZB significantly suppresses the phosphorylation of CAV-1 at a previously unreported Tyr42 site in HRECs. CAV1 is a major structural component of caveolae, small invaginations of the plasma membrane involved in a wide range of cellular functions, such as the membrane dynamics, lipid trafficking, and signal transduction [48]. It is reported to regulate the turnover of TGFβ type 1 receptors, promote their degradation, thereby terminating TGFβ signalling [64]. Indeed, we observed an elevated expression of the anti-angiogenic TGFβ type I receptor ALK5 and increased cytoplasmic accumulation of its downstream signalling transducer Smad3 in FRZB-treated HRECs. We further demonstrated a

critical role of Tyr42 phosphorylation in Cav-1 in FRZB-mediated HREC activation, angiogenesis, and TGFβ signalling.

Cav-1 is expected to form a disc-like structure sitting within the cytoplasmic leaflet of the plasma membrane, with residues 44 to 178 participating directly in Cav-1 oligomer assembly, while the N-terminal sequences extend into the cytoplasm, free to interact with other signalling proteins [65]. To understand how FRZB, a secreted protein, could influence the phosphorylation of CAV-1 at Try42, a residue located in the cytoplasmic arm of CAV-1, we performed a co-immunoprecipitation assay on the lysate and supernatant of CAV-1 and FRZB overexpressing HRECs and demonstrated physical interaction between FRZB and CAV-1 only in the extracellular milieu. Although CAV-1 has long been known as a plasma membrane protein, it could be secreted by various types of cells, in extracellular vesicles [49,66-68]. While predominantly present in the lumen of the vesicles, a recent study provided compelling evidence supporting an inverted CAV-1 topology on the vesicle membrane [69], making it accessible to other secreted molecules. The interaction between CAV-1 and FRZB was further supported by AlphaFold3 [70] modelling, which positions Tyr42 at the FRZB-CAV-1 interface and highlights its role in maintaining the stability of the CAV-1 and FRZB complex. The loss of the anti-angiogenic activity of FRZB in CAV-1 Y42D overexpressing HRECs underscores the functional relevance of this binding site. Given the abundant expression of CAV-1 in the eye and its role in vascular dysfunction [71-75], our findings place CAV-1 as a key molecular node in FRZB-mediated ocular angiogenesis and vascular leakage. Beyond its mechanistic novelty, FRZB demonstrates robust therapeutic potential. Both full-length FRZB and its NTR domain not only prevented pathological ocular neovascularization but also induced regression of established lesions in multiple preclinical models, without affecting physiological angiogenesis. Moreover, Fc-NTR exhibited efficacy comparable to Aflibercept and

acted synergistically when used in combination, suggesting a complementary mechanism that could enhance the current anti-VEGF standard of care. The selectivity for pathological angiogenesis, coupled with activity in regression, addresses a critical gap in existing therapies, especially sub-optimal treatment outcomes and potential long-term toxicity associated with existing VEGF inhibitors.

The implication of our findings extends beyond ocular disease. Epigenetic analysis implicates FRZB as a key molecular player in geographic atrophy (GA), a late stage "dry" form of AMD [76]. Reduced FRZB expression has also been reported in various tumours [77-79], osteoarthritis [80,81], abdominal aortic aneurysm [82], myelodysplastic syndromes [83], and atherosclerosis [84]. Functional studies indicate that FRZB knockdown promotes the aggressiveness of cancer cells [85] and the phenotypic switch of vascular smooth muscle cells [86], while FRZB overexpression suppresses tumour growth and invasiveness [87-89]. High FRZB levels also significantly correlate with a favourable prognosis in breast carcinoma [90]. These observations suggest that FRZB-based therapeutics could be applied to a spectrum of vascular disorders.

In conclusion, we define FRZB as a VEGF-, FGF2-, and Wnt-independent regulator of angiogenesis and vascular leakage that acts through extracellular engagement of CAV-1 and suppression of its phosphorylation to potentiate ALK5-Smad3 signalling (Fig. 6). This work expands the functional repertoire of sFRPs and uncovers a previously unrecognised molecular mechanism for angiogenesis control. Future studies should address how FRZB-Cav-1 interaction is regulated in diseases, whether other cofactors participate in this axis, and the translational potential of NTR-based biologics in systemic angiogenic diseases.

A key limitation of the present study is the use of global *Frzb*$^{-/-}$ mice rather than mice with cell type-specific deletion of *Frzb*. Although our RNAscope analyses and publicly available single-

cell RNA-sequencing datasets indicate that FRZB expression is predominantly restricted to Müller cells in the retina of both mice and humans, the potential contribution of other cell types to the observed vascular phenotype cannot be entirely excluded. Future studies employing conditional knockout approaches to selectively delete *Frzb* in Müller cells or endothelial cells will be valuable to delineate the cell–type–specific mechanisms underlying FRZB's role in ocular angiogenesis. In addition, while no significant changes in the expression of key angiogenic genes (*Vegf*, *Fgf2*, and *Wnt* pathway components) were detected in *Frzb*-deficient ocular tissues, the protein-level validation was not performed, and thus, we cannot fully exclude their involvement in FRZB-regulated ocular angiogenesis. Finally, although the OIR and CNV models are widely used to study pathological angiogenesis in the eye, the pathogenesis of multifactorial diseases, such as PDR and nAMD, is considerably more complex, involving additional components, including chronic inflammation, metabolic dysregulation, and neurodegeneration. Continued advances in disease-relevant preclinical models and human-based analyses will be essential to inform the translational potential of FRZB-based therapeutics in the clinical setting.

Methods

Human PDR patient specimen

The human study followed the ethical guidelines of the WMA Declaration of Helsinki and was approved by the local institutional review board (SingHealth cIRB 2015/2672).

Vitreous samples were collected from patients with proliferative diabetic retinopathy (PDR) undergoing vitreoretinal surgery for tractional retinal detachment. Patients with epiretinal membranes (ERM) or retinal detachment (RD) requiring surgery due to significant visual impairment, but without observable active retinal vascular disease, served as controls. Written

informed consent was obtained before the procedure. During trans pars plana vitrectomy, vitreous samples (500 μl) were aspirated at the start of the surgery using a vitreous cutter, with the infusion turned off to prevent sample dilution. The collected samples were immediately placed on ice and transported to the laboratory under a cold chain. Upon arrival, the samples were centrifuged at 4°C to remove cellular debris and subsequently stored at -80°C until downstream analysis.

Animals

Animal experiments were performed in compliance with the guidelines of the Institutional Animal Care and Use Committee of the Agency for Science, Technology, and Research (A*STAR) (181334), Singapore Eye Research Institute (SERI) (1135, 2014/SHS/0911, and 2020/SHS/1597) and the Association for Research in Vision and Ophthalmology Statement for the Use of Animals in Ophthalmic and Vision Research.

Animals were housed in the SingHealth Experimental Medicine Centre (SEMC) animal facility and were exposed to a standard 12-hour light-dark cycle. C57BL/6J mice were purchased from Invivos (Singapore). *Frzb*$^{-/-}$ mice were generated by the University of California Davies knockout mouse project (KOMP) repository (http://www.komp.org/) (Supplementary Fig. 13). Male Dutch Belted pigmented rabbits were obtained from Covance (Covance Research Products Inc., Denver, PA).

Mouse model of laser-induced choroidal neovascularization

6- to 8-week-old mice were subjected to laser-induced CNV. Before laser photocoagulation, an appropriate amount of ketamine/xylazine cocktail was administered to the mice according to their body weight by IP injection. Laser photocoagulation was performed using the image-guided laser system (Micron IV, Phoenix Research Laboratories, Pleasanton, CA, USA). Four laser burns were placed in each eye at 3, 6, 9, and 12 o'clock positions with equal distances from the optic disc,

using a green Argon laser pulse with wavelength 532 nm, diameter 50 μm, duration 50 ms, and power 120 mW. The lesions were evaluated by FFA and OCT at post-laser day 7 and day 14. After the evaluation, mice were sacrificed, and the eyes were enucleated. The RPE-choroid-sclera complex was isolated and snap-frozen for further analysis ($n \geq 5$ animals per group).

Oxygen-induced retinopathy (OIR) model

Postnatal day 7 pups and their nursing mother were placed in the oxygen chamber supplied with 75% oxygen and exposed to a standard 12-hour light-dark cycle from postnatal day 7 to day 12. The nursing mothers were removed from the chamber and allowed to recover in room air for 1 to 2 hours every day. All mice were returned to room air on postnatal day 12 and were further kept until postnatal day 17. The pups were sacrificed on postnatal day 17, and the retinae were isolated and snap-frozen for further analysis. Age-matched normoxic (NOR) pups were used as controls ($n \geq 5$ animals per group).

Rabbit model of persistent retinal neovascularization

Persistent Retinal Neovascularization (PRNV) Rabbit model was established as described [29]. In brief, PRNV was induced by a single intravitreal injection of 50 μL of 0.025 M DL-2-aminoadipic acid (DL-AAA) per eye of adult Dutch Belted pigmented rabbits (around 6 months old). The establishment of PRNV was confirmed by fluorescein angiography. Fc-NTR or vehicle was delivered intravitreally 12 weeks after the first DL-AAA injection. Fluorescein angiography (FFA) was used to evaluate retinal vascular leakage weekly after the treatment and was normalized to baseline fluorescein levels ($n = 3$ animals per group).

Intravitreal injections

Mice were anesthetized with an appropriate amount of ketamine/xylazine cocktail by intraperitoneal injection. 0.5% proparacaine hydrochloride (Alcon) was applied to the corneal

surface for topical anaesthesia of the eyes. One drop of 1% tropicamide (Alcon Laboratories, Inc., Tampa, FL) followed by phenylephrine (2.5%; Bausch and Lomb Pharmaceuticals, Inc., Tampa, FL) was applied to dilate the pupils. A 33-gauge needle (Hamilton, Switzerland) was used for the delivery of ocular therapeutics and vehicle control into the vitreous cavity.

Fundus photography, Fundus Fluorescein Angiography (FFA), and Optical Coherence Tomography (OCT)

Digital colour fundus photography, FFA, and OCT were performed using the Micron IV Retinal Imaging Microscope (Phoenix Research Laboratory) after topical administration of one drop of 1% tropicamide (Alcon Laboratories, Inc., Tampa, FL), followed by one drop of 2.5% phenylephrine (Bausch and Lomb Pharmaceuticals, Inc., Tampa, FL) ophthalmic solutions for pupil dilation. For FFA, mice were injected intraperitoneally with 10% sodium fluorescein dye at a dose of 0.01 mL/5-6 g body weight after pupil dilation. The passage of fluorescein through the retinal vascular system was serially recorded using a fundus camera equipped with exciter and barrier filters suitable for FFA. The images were used for examining retinal microvascular characteristics.

Choroid sprouting assay

The choroid sprouting assay was performed as described [91]. In brief, eyes were enucleated from one-week-old C57BL/6J mice, and the RPE/choroid tissues were dissected, cut into ~1 mm^2 explants, and embedded in the growth factor–reduced (GFR) Matrigel. For the prevention study, vehicle control and treatment medium were added to the explants on the day of embedding, and the media were changed every other day. Images were taken after 4 days of treatment. For the regression assay, choroidal explants were allowed to grow for 2 days before being subjected to respective treatments for 2 more days. Vessel outgrowth was visualized under the Eclipse Ti-E

Inverted Research Microscope (Nikon, Japan). The sprouting area was quantified using Image J software (n ≥ 8 explants per group).

Metatarsal assay

The metatarsal assay was performed as described [91]. In brief, metatarsal bones were isolated from E16.5 C57BL/6J mice and seeded onto gelatine-coated 24-well plates. Fc-NTR (500 µM), Fc-FRZB (500 nM), or vehicle control was added to explants 2 days after embedding. The media were changed every other day. At day 10 of culture, the explants were fixed in 4% PFA before being incubated with CD31 antibody (rat monoclonal, BD Biosciences, Cat# 550274, Lot# 1207300) and NG2 antibody (rabbit polyclonal, Millipore, Cat# AB5320, Lot# 3284258), followed by staining with secondary antibodies. Vessel outgrowth from metatarsals was visualized under the Eclipse Ti-E Inverted Research Microscope (Nikon, Japan) and quantified using TRI2 software (https://app.assembla.com/spaces/ATD_TRI/wiki) (n ≥ 8 explants per group).

Aortic ring assay

Aortic ring assay was performed as described[91]. The aorta from postnatal day 3 (P3) C57BL/6J mice was cut into 1mm rings before being embedded in a 96-well plate coated with rat tail collagen I gel (BD). Culture medium containing Fc-NTR (500 µM), Fc-FRZB (500 nM), or vehicle control with 1.8 nM VEGF was added to explants after collagen I gel was polymerized. Treatment media were changed every other day. At day 10 of culture, the explants were fixed in 4% PFA and stained with Griffonia Simplicifolia Lectin (GSL) isolectin IB4 (Invitrogen, Cat# I32450, Lot# 2155275) and AN2-PE (rat monoclonal, Miltenyi Biotec, Cat# 130-100-468, Lot# n/a). Vessel outgrowth was visualized under the Eclipse Ti-E Inverted Research Microscope (Nikon, Japan). The number of spouts was counted manually (n ≥ 8 explants per group).

Cells and Cell Culture

Primary human retinal endothelial cells (HREC, cAP-0010), human retinal pigment epithelial cells (HPRE, cAP-0037), and human retinal pericyte (cAP-0025) were purchased from Angioproteomie (MA, USA) and maintained in EGM2 Endothelial Cell Growth Medium (Lonza, CC-3162), HRPECs Growth Medium (Angioproteomie, cAP-45C), and Pericyte Growth Medium (Angioproteomie, cAP-09), respectively, according to the supplier's instructions. Human Müller cells (MIO-M1) were cultured in DMEM high glucose (Thermo, 11965092) supplemented with 10% foetal bovine serum [92].

Expi293F cells (Gibco, A14527) were cultured in Expi293 Expression Medium (Gibco, A1435101) and used to produce Fc-FRZB, Fc-CRD, and Fc-NTR recombinant proteins. ExpiFectamine 293 (Gibco, A14525) transfection reagent was used to transiently transfect Fc-FRZB, Fc-CRD, and Fc-NTR plasmids following the manufacturer's protocol. The culture was incubated at 37 °C, 8.0% CO2, at a speed of 120 rpm with an orbit diameter of 25 mm. Expression enhancers were added 16 hours following the transfection. Cell viability was monitored by using Countess II Cell Counters (Invitrogen). Once cell viability was below 70%, the spent media was collected for chimeric protein purification using a His-tag affinity column, followed by Gel filtration.

Mass spectrometry analysis

Two different clinical vitreous sample sets were subjected to two different mass spectrometry-based proteomics approaches, namely SWATH-MS and Tandem Mass Tag (TMT) labelling. For SWATH-MS analysis, the tryptic-digested vitreous samples were subjected to NanoLC-MS/MS (Ultimate 3000 nanoLC system coupled with AB Sciex 5600 TripleTOF). The raw data analysis was processed using the SWATH data processing package in PeakView (Sciex, Framingham, MA, USA). Data were exported for further analysis using R (Foundation for Statistical Computing, Vienna, Austria). Quantitative phosphoproteomics analysis was performed using a TMT-based

approach using Fc-FRZB-treated cell lysate in comparison to controls. The resulting MS/MS data were analysed using Scientific Proteome Discoverer version 2.5 (Thermo Fisher Scientific, Massachusetts, USA), employing the Sequest HT search engine for phosphoproteomics. MS Amanda 2.0 for phosphoproteomics and protein identification was filtered based on a 1% FDR to ensure high-confidence results. The phosphosite localization score filter was set at 0.75. Raw intensities were log2-transformed and normalized across a TMT set using median normalization. All experimental details, including data analysis parameters, are described under supplemental methods.

Molecular Biological Methods

The coding sequence (33-325 aa) of human FRZB (NM_001463.4), its CRD domain (33-157 aa), and its NTR domain (167-325 aa) were cloned into the pHLmFc plasmid[93] (a gift from Markus Ralser; Addgene plasmid # 64168; http://n2t.net/addgene:64168; RRID: Addgene_64168) at the KpnI restriction site (Supplementary Fig. 8A-B) to form Fc-FRZB, Fc-CRD, and Fc-NTR expression vectors. The recombinant human proteins were expressed in Expi293 cells (Gibco, A14527). The coding sequence of the human CAV1 (NM_001172895.1) was cloned into pcDNA™3.1 (+) (Invitrogen, catalogue: V79020) at the HindIII/BamHI sites to form pcDNA-CAV1. CAV Y14D and CAV Y42D mutant plasmids were generated by replacing Tyr 14 and Tyr 42 with Asp (DNA sequence TAC to GAC) of the CAV1, respectively (Supplementary Fig. 14).

Purification of recombinant proteins

Smart Ni-NTA resin (Bio Basic), equilibrated as a 50% slurry in conditioning buffer (5× stock: 100 mM HEPES pH 7.5, 150 mM NaCl, 25 mM imidazole, 2.5% glycerol, 1× protease inhibitor cocktail), was used to purify Fc-FRZB, Fc-CRD, and Fc-NTR. After one hour incubation with gentle agitation at 4 ºC, the resin was washed with IMAC buffer (50 mM HEPES pH 7.5, 300 mM

NaCl, 10% glycerol) containing increasing imidazole concentrations and eluted with buffer containing 500 mM imidazole. The eluant was exchanged into PBS using a PD-10 desalting column (GE Healthcare) that was pre-equilibrated in storage buffer (20 mM HEPES, pH 7.5, 300 mM NaCl, 10% glycerol). The protein was subsequently concentrated using a Vivaspin centrifugal concentrator (Sartorius) with a 30 kDa molecular weight cut-off. The final protein concentration was determined using Nanodrop (ThermoFisher).

SDS PAGE and Western blotting

Total protein was extracted from cells and tissues using Tortex lysis buffer (20 mM HEPES, pH 7.9, 350 mM NaCl, 20% v/v glycerol, 1% NP-40, 1 mM $MgCl_2$, 0.5 mM EDTA, 0.1 mM EGTA) with freshly added protease inhibitor (Roche) and phosphatase inhibitor (Roche). Proteins were separated by SDS-PAGE before being transferred onto a PVDF membrane (Merck Millipore, USA). The blots were probed with FRZB (rabbit monoclonal, Abcam, Cat# ab273582, Lot# GR3347459-3), VEGF Receptor 2 (rabbit monoclonal, CST, Cat# 2479S, Lot# 18), Phospho-VEGF Receptor 2 (rabbit monoclonal, CST, Cat# 2478S, Lot# 16), SMAD3 (rabbit monoclonal, CST, Cat# 9523S, Lot# 5), Phospho-SMAD3 (rabbit monoclonal, CST, Cat# 9520S, Lot# 16), SMAD1/5 (mouse monoclonal, Abcam, Cat# ab75273, Lot# GR3278248-1), Phospho-SMAD1/5 (rabbit monoclonal, CST, Cat# 9516S, Lot# 9), ALK-1 (rat monoclonal, Santa Cruz, Cat# sc-101556, Lot# B2813), ALK-5 (rabbit polyclonal, Sigma, Cat# SAB4502958, Lot# 211126), CAV1 (rabbit monoclonal, CST, Cat# 3267S, Lot# 94), β-Catenin (rabbit monoclonal, CST, Cat# 8814S, Lot# 4), LRP6 (rabbit monoclonal, CST, Cat# 3395S, Lot# 3), Phospho-LRP6 (rabbit polyclonal, CST, Cat# 2568S, Lot# 6) or GAPDH (mouse monoclonal, Proteintech, 60004-1-Ig, Lot# 00122627) antibodies, followed by horseradish peroxidase (HRP)-conjugated secondary antibodies (Santa Cruz Biotechnology). Densitometry was performed using ImageJ.

Co-Immunoprecipitation

FRZB and CAV1 were co-transfected into HEK293 cells, which were cultured in T75 flasks. On day 5 post-transfection, the cell lysates and culture supernatants were collected for analysis. The culture supernatant was concentrated from 10 mL to 1 mL using Amicon® Ultra-15 Centrifugal Filters (Ultracel-30k, UFC903024). Total protein from the cell lysate (equivalent to half a T75 flask at full confluency) was extracted using 600 µL of Pierce™ IP Lysis Buffer.

For immunoprecipitation (IP), 200 µL of the lysate extract and the concentrated supernatant were pre-cleared by incubating with Protein G Sepharose beads (Abcam, ab193259) for 1 hour at 4°C under rotary agitation to remove non-specific protein binding. Following pre-clearing, CAV1 antibody (rabbit monoclonal, CST, Cat# 3267S, Lot# 9) was added according to the manufacturer's instructions and incubated overnight at 4°C. Subsequently, 30 µL of Protein G Sepharose beads were added to the samples and incubated overnight at 4°C to pull down the antibody-conjugated protein complexes.

After incubation, the Sepharose beads were washed three times with lysis buffer to remove unbound proteins, followed by centrifugation to collect the beads. The protein-bound beads were resuspended in 40 µL of loading buffer and boiled at 95°C for 5 minutes to dissociate the conjugated proteins from the beads. After centrifugation, the supernatant containing the eluted proteins was collected for analysis.

Quantitative Real-time PCR (qRT-PCR)

RNA was extracted using an RNA extraction kit (QIAGEN, RNeasy Mini Kit) and was reverse transcribed into cDNA using qScript cDNA Synthesis Kit (Quantabio). PCR was conducted with QuantiTect Power SYBR Green (Applied Biosystems). Gene expression was normalized to *Gapdh* ($n \geq 4$ independent experiments). Primers used in this study are listed in Supplementary Table 1.

Proliferation assay

$2x10^3$ HRECs were cultured in EGM2 Endothelial Cell Growth Medium (Lonza, CC-3162) overnight. HRECs were then treated with 500 nM Fc-FRZB, Fc-CRD, Fc-NTR, and vehicle control for 24 hours, followed by incubation with Alamar Blue (Life Technology, USA) solution for another 4 hours. The colorimetric signal was captured by a Synergy H1 microplate reader (BioTek, USA). The proliferation rate in the treatment group was normalized to vehicle-treated controls (n = 3 independent experiments).

Matrigel tube formation assay

HRECs cultured in EGM2 Endothelial Cell Growth Medium (Lonza, CC-3162) containing 500 nM Fc-FRZB, Fc-CRD, Fc-NTR, or vehicle controls were seeded on top of polymerized GFR Matrigel (BD Biosciences, Oxford, UK). Images were taken 16 hours later using the Eclipse Ti-E Inverted Research Microscope (Nikon, Japan) and analysed using Image J Angiogenesis Analyzer (Gilles Carpentier). The fluorescence intensity was analysed by ImageJ ($n \geq 3$ independent experiments).

THP1 adhesion assay

HREC monolayers were treated with 500 nM Fc-FRZB, Fc-CRD, Fc-NTR, or vehicle control, respectively, for 24 hours, followed by stimulation with 50 ng/mL TNFα (PeproTech®, #300-01A-50UG) for another 2 hours. THP1 cells (ATCC, TIB-202) were labelled with Cell tracker CMFDA (Invitrogen, C7025) for 30 minutes and washed with Starving media (Gibco) two times before being added to the pre-treated HREC monolayer. Non-adherent THP1 cells were washed away with EGM2 media two hours later. The attached THP1 cells were imaged under the Eclipse Ti-E Inverted Research Microscope (Nikon, Japan). The fluorescent intensity of adhered THP1

cells was determined by a Synergy H1 microplate reader (BioTek, USA) (n = 5 independent experiments).

Migration assay

HRECs were seeded on 8.0 μm Transwell inserts (Corning, 3422) according to the supplier's instructions and were treated with 500 nM Fc-NTR, Fc-CRD, Fc-FRZB, or vehicle control for 4hours. After the incubation, the non-migrated cells were removed from the upper side of the membrane. The migrated cells were fixed with 4% PFA and stained with DAPI. Images were taken using an Eclipse Ti-E Inverted Research Microscope (Nikon, Japan) and were analysed using ImageJ ($n \geq 4$ independent experiments).

Retina/RPE Flatmount and Immunofluorescence Staining

Retina/RPE flatmounts were collected and fixed as previously described [94]. In brief, Retina/RPE flat-mounts were washed in 2 x PBS for 5 minutes before being incubated in the blocking buffer (1x PBS with 0.5% BSA, 3% Triton-X, and 1% Tween 20) for at least 1 hour. Retina/RPE flatmounts were then included in blocking buffer containing primary antibody against mouse CD31 (1:200, rat monoclonal, BD Biosciences, Cat# 550274, Lot# 1207300) at 4ºC overnight before being incubated in blocking buffer containing Alexa 488 secondary antibodies (1:200, Invitrogen, Cat# A11006, Lot# 2747446) for 2 hours. ImageJ was used to quantify the vascular area.

Secondary Structure Assignment and Sequence Preparation

Secondary structure assignments for FRZB and CAV1 were computed using JPred4[95]. Both sequences were also screened for the presence of an endoplasmic reticulum (ER) retention SignalP-4.1[96]. FRZB was found to contain an N-terminal signal peptide (residues 1-32) and a

predicted disordered region (residues 299-325). These regions were removed prior to structure modelling to improve model quality and focus on structured domains.

FRZB-CAV1 complex modelling

The structure models for FRZB (residue 33-298) and CAV1 were generated using AlphaFold3 [70]. For each protein, 75 structure models were generated using 15 different seeds (five models per seed). Subsequently, the top models for both proteins with the highest-ranking score were selected for complex generation using protein-protein docking. Protein-protein docking was performed with HADDOCK3 [97] using a multi-stage workflow. First, rigid-body docking was carried out, generating 2,000 random orientations using both surface restraints and centre-of-mass restraints, along with ambiguous interaction restraints targeting residues 1-60 of CAV1 and the entire FRZB (residue 33-298) protein. The top 1,000 models were selected for further refinement using semi-flexible simulated annealing with ambiguous interaction restraints. This was followed by scoring of the complexes through energy minimization without restraints. Final models were clustered based on interface contacts and ranked according to their scores. The models from the highest-scoring cluster were selected for subsequent analysis.

Structure Preparation and Mutagenesis

The selected top complex models were prepared using the Schrödinger Protein Preparation Wizard [98]. The preparation workflow included optimization of hydrogen-bonding networks and assignment of protonation states for all ionizable residues at physiological pH. The structures were then minimized to relieve any steric clashes or strain. Subsequently, site-directed mutagenesis was performed *in silico* to generate desired variants of CAV1.

Binding Free Energy Calculations

To estimate the effect of mutations, binding free energies of the wild-type and mutant FRZB-CAV1 complexes were estimated using Molecular Mechanics Generalized Born Surface Area (MM-GBSA) calculations using Schrödinger Prime (Schrodinger: Prime. LLC; New York, NY: 2025). For each complex, the residue at the mutated position (both the wild-type and mutant) in CAV1, along with neighbouring residues within 8 Å, was first optimized in an implicit water environment using the VSGB2.1 solvent model. Subsequently, MM-GBSA calculations were performed using the same implicit solvent model. To account for conformational flexibility, this procedure was repeated for all selected complex models, and the binding free energies were averaged. The effects of the mutations were evaluated by calculating the change in binding free energy (ΔΔG), defined as the difference between the average binding free energy of the wild-type and mutant complexes ($\Delta\Delta G = \langle \Delta G_{MUT} \rangle - \langle \Delta G_{WT} \rangle$).

Statistics

Data are expressed as the mean ± standard deviation (s.d.). Statistical analyses were conducted using an unpaired, two-tailed Student's t-test or one-way ANOVA, followed by an appropriate post-hoc test, utilizing Prism 5 software (GraphPad Software Inc.). * $p < 0.05$; ** $p < 0.01$; *** $p < 0.001$. Detailed statistical information for each experiment, including sample sizes (n), is provided in the corresponding figure legends.

Data Availability

Source data with specific *p-values* for all figures are provided with this paper. The mass spectrometry proteomics data have been deposited to the ProteomeXchange Consortium *via* the PRIDE partner repository with the dataset identifiers PXD036033 [https://www.ebi.ac.uk/pride/archive/projects/PXD036033], PXD073342 [https://www.ebi.ac.uk/pride/archive/projects/PXD073342], and PXD073005

[https://www.ebi.ac.uk/pride/archive/projects/PXD073005]. Additional details on datasets and protocols that support the findings of this study will be made available by the corresponding author upon request.

References

1 Carmeliet, P. Angiogenesis in health and disease. *Nat Med* **9**, 653-660 (2003). https://doi.org:10.1038/nm0603-653

2 Teo, Z. L. *et al.* Global Prevalence of Diabetic Retinopathy and Projection of Burden through 2045: Systematic Review and Meta-analysis. *Ophthalmology* **128**, 1580-1591 (2021). https://doi.org:10.1016/j.ophtha.2021.04.027

3 Wong, W. L. *et al.* Global prevalence of age-related macular degeneration and disease burden projection for 2020 and 2040: a systematic review and meta-analysis. *Lancet Glob Health* **2**, e106-116 (2014). https://doi.org:10.1016/S2214-109X(13)70145-1

4 Perez-Gutierrez, L. & Ferrara, N. Biology and therapeutic targeting of vascular endothelial growth factor A. *Nat Rev Mol Cell Biol* **24**, 816-834 (2023). https://doi.org:10.1038/s41580-023-00631-w

5 Mettu, P. S., Allingham, M. J. & Cousins, S. W. Incomplete response to Anti-VEGF therapy in neovascular AMD: Exploring disease mechanisms and therapeutic opportunities. *Prog Retin Eye Res* **82**, 100906 (2021). https://doi.org:10.1016/j.preteyeres.2020.100906

6 Binder, S. Loss of reactivity in intravitreal anti-VEGF therapy: tachyphylaxis or tolerance? *Br J Ophthalmol* **96**, 1-2 (2012). https://doi.org:10.1136/bjophthalmol-2011-301236

7 Abdullah, S. E. & Perez-Soler, R. Mechanisms of resistance to vascular endothelial growth factor blockade. *Cancer* **118**, 3455-3467 (2012). https://doi.org:10.1002/cncr.26540

8 Dejana, E. The role of wnt signaling in physiological and pathological angiogenesis. *Circ Res* **107**, 943-952 (2010). https://doi.org:10.1161/CIRCRESAHA.110.223750

9 Toomes, C. *et al.* Mutations in LRP5 or FZD4 underlie the common familial exudative vitreoretinopathy locus on chromosome 11q. *Am J Hum Genet* **74**, 721-730 (2004). https://doi.org:10.1086/383202

10 Ohlmann, A., Seitz, R., Braunger, B., Seitz, D., Bosl, M. R. & Tamm, E. R. Norrin promotes vascular regrowth after oxygen-induced retinal vessel loss and suppresses retinopathy in mice. *J Neurosci* **30**, 183-193 (2010). https://doi.org:10.1523/JNEUROSCI.3210-09.2010

11 Post, Y. *et al.* Design principles and therapeutic applications of novel synthetic WNT signaling agonists. *iScience* **27**, 109938 (2024). https://doi.org:10.1016/j.isci.2024.109938

12 Chidiac, R. *et al.* A Norrin/Wnt surrogate antibody stimulates endothelial cell barrier function and rescues retinopathy. *EMBO Mol Med* **13**, e13977 (2021). https://doi.org:10.15252/emmm.202113977

13 Zhang, X., Dong, N. & Hu, X. Wnt/beta-catenin Signaling Inhibitors. *Curr Top Med Chem* **23**, 880-896 (2023). https://doi.org:10.2174/1568026623666230303101810

14 Xavier, C. P., Melikova, M., Chuman, Y., Uren, A., Baljinnyam, B. & Rubin, J. S. Secreted Frizzled-related protein potentiation versus inhibition of Wnt3a/beta-catenin signaling. *Cell Signal* **26**, 94-101 (2014). https://doi.org:10.1016/j.cellsig.2013.09.016

15 Galli, L. M. *et al.* Differential inhibition of Wnt-3a by Sfrp-1, Sfrp-2, and Sfrp-3. *Dev Dyn* **235**, 681-690 (2006). https://doi.org:10.1002/dvdy.20681

16 Alfaro, M. P. *et al.* sFRP2 suppression of bone morphogenic protein (BMP) and Wnt signaling mediates mesenchymal stem cell (MSC) self-renewal promoting engraftment and myocardial repair. *J Biol Chem* **285**, 35645-35653 (2010). https://doi.org:10.1074/jbc.M110.135335

17 von Marschall, Z. & Fisher, L. W. Secreted Frizzled-related protein-2 (sFRP2) augments canonical Wnt3a-induced signaling. *Biochem Biophys Res Commun* **400**, 299-304 (2010). https://doi.org:10.1016/j.bbrc.2010.08.043

18 Uren, A. *et al.* Secreted frizzled-related protein-1 binds directly to Wingless and is a biphasic modulator of Wnt signaling. *J Biol Chem* **275**, 4374-4382 (2000). https://doi.org:10.1074/jbc.275.6.4374

19 Bovolenta, P., Esteve, P., Ruiz, J. M., Cisneros, E. & Lopez-Rios, J. Beyond Wnt inhibition: new functions of secreted Frizzled-related proteins in development and disease. *J Cell Sci* **121**, 737-746 (2008). https://doi.org:10.1242/jcs.026096

20 Alli-Shaik, A. *et al.* System-wide vitreous proteome dissection reveals impaired sheddase activity in diabetic retinopathy. *Theranostics* **12**, 6682-6704 (2022). https://doi.org:10.7150/thno.72947

21 Smith, L. E. *et al.* Oxygen-induced retinopathy in the mouse. *Invest Ophthalmol Vis Sci* **35**, 101-111 (1994).

22 Lambert, V. *et al.* Laser-induced choroidal neovascularization model to study age-related macular degeneration in mice. *Nat Protoc* **8**, 2197-2211 (2013). https://doi.org:10.1038/nprot.2013.135

23 Zuercher, J., Fritzsche, M., Feil, S., Mohn, L. & Berger, W. Norrin stimulates cell proliferation in the superficial retinal vascular plexus and is pivotal for the recruitment of mural cells. *Hum Mol Genet* **21**, 2619-2630 (2012). https://doi.org:10.1093/hmg/dds087

24 Xu, Q. *et al.* Vascular development in the retina and inner ear: control by Norrin and Frizzled-4, a high-affinity ligand-receptor pair. *Cell* **116**, 883-895 (2004). https://doi.org:10.1016/s0092-8674(04)00216-8

25 Ye, X. *et al.* Norrin, frizzled-4, and Lrp5 signaling in endothelial cells controls a genetic program for retinal vascularization. *Cell* **139**, 285-298 (2009). https://doi.org:10.1016/j.cell.2009.07.047

26 Bu, Q., Li, Z., Zhang, J., Xu, F., Liu, J. & Liu, H. The crystal structure of full-length Sizzled from Xenopus laevis yields insights into Wnt-antagonistic function of secreted Frizzled-related proteins. *J Biol Chem* **292**, 16055-16069 (2017). https://doi.org:10.1074/jbc.M117.791756

27 Ucuzian, A. A., Gassman, A. A., East, A. T. & Greisler, H. P. Molecular mediators of angiogenesis. *J Burn Care Res* **31**, 158-175 (2010). https://doi.org:10.1097/BCR.0b013e3181c7ed82

28 Noda, K., Nakao, S., Ishida, S. & Ishibashi, T. Leukocyte adhesion molecules in diabetic retinopathy. *J Ophthalmol* **2012**, 279037 (2012). https://doi.org:10.1155/2012/279037

29 Li, Y. *et al.* A novel model of persistent retinal neovascularization for the development of sustained anti-VEGF therapies. *Exp Eye Res* **174**, 98-106 (2018). https://doi.org:10.1016/j.exer.2018.05.027

30 Shibata, M., Itoh, M., Hikasa, H., Taira, S. & Taira, M. Role of crescent in convergent extension movements by modulating Wnt signaling in early Xenopus embryogenesis. *Mech Dev* **122**, 1322-1339 (2005). https://doi.org:10.1016/j.mod.2005.06.002

31 Mii, Y. & Taira, M. Secreted Frizzled-related proteins enhance the diffusion of Wnt ligands and expand their signalling range. *Development* **136**, 4083-4088 (2009). https://doi.org:10.1242/dev.032524

32 Leyns, L., Bouwmeester, T., Kim, S. H., Piccolo, S. & De Robertis, E. M. Frzb-1 is a secreted antagonist of Wnt signaling expressed in the Spemann organizer. *Cell* **88**, 747-756 (1997). https://doi.org:10.1016/s0092-8674(00)81921-2

33 Lin, K., Wang, S., Julius, M. A., Kitajewski, J., Moos, M., Jr. & Luyten, F. P. The cysteine-rich frizzled domain of Frzb-1 is required and sufficient for modulation of Wnt signaling. *Proc Natl Acad Sci U S A* **94**, 11196-11200 (1997). https://doi.org:10.1073/pnas.94.21.11196

34 Wang, S., Krinks, M. & Moos, M., Jr. Frzb-1, an antagonist of Wnt-1 and Wnt-8, does not block signaling by Wnts -3A, -5A, or -11. *Biochem Biophys Res Commun* **236**, 502-504 (1997). https://doi.org:10.1006/bbrc.1997.6995

35 Wang, S., Krinks, M., Lin, K., Luyten, F. P. & Moos, M., Jr. Frzb, a secreted protein expressed in the Spemann organizer, binds and inhibits Wnt-8. *Cell* **88**, 757-766 (1997). https://doi.org:10.1016/s0092-8674(00)81922-4

36 Huang, C. L. *et al.* Wnt1 overexpression promotes tumour progression in non-small cell lung cancer. *Eur J Cancer* **44**, 2680-2688 (2008). https://doi.org:10.1016/j.ejca.2008.08.004

37 Cheng, C. W., Smith, S. K. & Charnock-Jones, D. S. Wnt-1 signaling inhibits human umbilical vein endothelial cell proliferation and alters cell morphology. *Exp Cell Res* **291**, 415-425 (2003). https://doi.org:10.1016/j.yexcr.2003.07.006

38 Chakraborty, A. *et al.* Wnt7a deficit is associated with dysfunctional angiogenesis in pulmonary arterial hypertension. *Eur Respir J* **61** (2023). https://doi.org:10.1183/13993003.01625-2022

39 Lin, J. B. *et al.* WNT7A/B promote choroidal neovascularization. *Exp Eye Res* **174**, 107-112 (2018). https://doi.org:10.1016/j.exer.2018.05.033

40 Schevenels, G. *et al.* A brain-specific angiogenic mechanism enabled by tip cell specialization. *Nature* **628**, 863-871 (2024). https://doi.org:10.1038/s41586-024-07283-6

41 Wang, W., Yan, X., Lin, Y., Ge, H. & Tan, Q. Wnt7a promotes wound healing by regulation of angiogenesis and inflammation: Issues on diabetes and obesity. *J Dermatol Sci* (2018). https://doi.org:10.1016/j.jdermsci.2018.02.007

42 Manukjan, N. *et al.* Wnt7a Decreases Brain Endothelial Barrier Function Via beta-Catenin Activation. *Mol Neurobiol* **61**, 4854-4867 (2024). https://doi.org:10.1007/s12035-023-03872-0

43 Wang, Y. *et al.* Interplay of the Norrin and Wnt7a/Wnt7b signaling systems in blood-brain barrier and blood-retina barrier development and maintenance. *Proc Natl Acad Sci U S A* **115**, E11827-E11836 (2018). https://doi.org:10.1073/pnas.1813217115

44 Cho, C., Wang, Y., Smallwood, P. M., Williams, J. & Nathans, J. Molecular determinants in Frizzled, Reck, and Wnt7a for ligand-specific signaling in neurovascular development. *Elife* **8** (2019). https://doi.org:10.7554/eLife.47300

45 Cho, C., Smallwood, P. M. & Nathans, J. Reck and Gpr124 Are Essential Receptor Cofactors for Wnt7a/Wnt7b-Specific Signaling in Mammalian CNS Angiogenesis and Blood-Brain Barrier Regulation. *Neuron* **95**, 1221-1225 (2017). https://doi.org:10.1016/j.neuron.2017.08.032

46 Muley, A. *et al.* Secreted frizzled-related protein 4: an angiogenesis inhibitor. *Am J Pathol* **176**, 1505-1516 (2010). https://doi.org:10.2353/ajpath.2010.090465

47 Siamakpour-Reihani, S. *et al.* The role of calcineurin/NFAT in SFRP2 induced angiogenesis--a rationale for breast cancer treatment with the calcineurin inhibitor tacrolimus. *PLoS One* **6**, e20412 (2011). https://doi.org:10.1371/journal.pone.0020412

48 Parton, R. G. Caveolae: Structure, Function, and Relationship to Disease. *Annu Rev Cell Dev Biol* **34**, 111-136 (2018). https://doi.org:10.1146/annurev-cellbio-100617-062737

49 Tahir, S. A. *et al.* Secreted caveolin-1 stimulates cell survival/clonal growth and contributes to metastasis in androgen-insensitive prostate cancer. *Cancer Res* **61**, 3882-3885 (2001).

50 Liu, P., Li, W. P., Machleidt, T. & Anderson, R. G. Identification of caveolin-1 in lipoprotein particles secreted by exocrine cells. *Nat Cell Biol* **1**, 369-375 (1999). https://doi.org:10.1038/14067

51 Inder, K. L. *et al.* Cavin-1/PTRF alters prostate cancer cell-derived extracellular vesicle content and internalization to attenuate extracellular vesicle-mediated osteoclastogenesis and osteoblast proliferation. *J Extracell Vesicles* **3** (2014). https://doi.org:10.3402/jev.v3.23784

52 Logozzi, M. *et al.* High levels of exosomes expressing CD63 and caveolin-1 in plasma of melanoma patients. *PLoS One* **4**, e5219 (2009). https://doi.org:10.1371/journal.pone.0005219

53 Simon, L., Campos, A., Leyton, L. & Quest, A. F. G. Caveolin-1 function at the plasma membrane and in intracellular compartments in cancer. *Cancer Metastasis Rev* **39**, 435-453 (2020). https://doi.org:10.1007/s10555-020-09890-x

54 Crewe, C. *et al.* An Endothelial-to-Adipocyte Extracellular Vesicle Axis Governed by Metabolic State. *Cell* **175**, 695-708 e613 (2018). https://doi.org:10.1016/j.cell.2018.09.005

55 Gherghe, C. M. *et al.* Wnt1 is a proangiogenic molecule, enhances human endothelial progenitor function, and increases blood flow to ischemic limbs in a HGF-dependent manner. *FASEB J* **25**, 1836-1843 (2011). https://doi.org:10.1096/fj.10-172981

56 Rodriguez, J. *et al.* SFRP1 regulates the growth of retinal ganglion cell axons through the Fz2 receptor. *Nat Neurosci* **8**, 1301-1309 (2005). https://doi.org:10.1038/nn1547

57 Oshima, T. *et al.* Myeloma cells suppress bone formation by secreting a soluble Wnt inhibitor, sFRP-2. *Blood* **106**, 3160-3165 (2005). https://doi.org:10.1182/blood-2004-12-4940

58 He, W. *et al.* Exogenously administered secreted frizzled related protein 2 (Sfrp2) reduces fibrosis and improves cardiac function in a rat model of myocardial infarction. *Proc Natl Acad Sci U S A* **107**, 21110-21115 (2010). https://doi.org:10.1073/pnas.1004708107

59 Kobayashi, K. *et al.* Secreted Frizzled-related protein 2 is a procollagen C proteinase enhancer with a role in fibrosis associated with myocardial infarction. *Nat Cell Biol* **11**, 46-55 (2009). https://doi.org:10.1038/ncb1811

60 Misra, K. & Matise, M. P. A critical role for sFRP proteins in maintaining caudal neural tube closure in mice via inhibition of BMP signaling. *Dev Biol* **337**, 74-83 (2010). https://doi.org:10.1016/j.ydbio.2009.10.015

61 Park, K. W. *et al.* The axonal attractant Netrin-1 is an angiogenic factor. *Proc Natl Acad Sci U S A* **101**, 16210-16215 (2004). https://doi.org:10.1073/pnas.0405984101

62 Fan, Y. *et al.* Overexpression of netrin-1 induces neovascularization in the adult mouse brain. *J Cereb Blood Flow Metab* **28**, 1543-1551 (2008). https://doi.org:10.1038/jcbfm.2008.39

63 Tu, T. *et al.* CD146 acts as a novel receptor for netrin-1 in promoting angiogenesis and vascular development. *Cell Res* **25**, 275-287 (2015). https://doi.org:10.1038/cr.2015.15

64 Di Guglielmo, G. M., Le Roy, C., Goodfellow, A. F. & Wrana, J. L. Distinct endocytic pathways regulate TGF-beta receptor signalling and turnover. *Nat Cell Biol* **5**, 410-421 (2003). https://doi.org:10.1038/ncb975

65 Parton, R. G. & Collins, B. M. The structure of caveolin finally takes shape. *Sci Adv* **8**, eabq6985 (2022). https://doi.org:10.1126/sciadv.abq6985

66 Tahir, S. A. *et al.* Tumor cell-secreted caveolin-1 has proangiogenic activities in prostate cancer. *Cancer Res* **68**, 731-739 (2008). https://doi.org:10.1158/0008-5472.CAN-07-2668

67 Chang, C. C. *et al.* Caveolin-1 Secreted from Adipose Tissues and Adipocytes Functions as an Adipogenesis Enhancer. *Obesity (Silver Spring)* **25**, 1932-1940 (2017). https://doi.org:10.1002/oby.21970

68 Campos, A. *et al.* Caveolin-1-containing extracellular vesicles transport adhesion proteins and promote malignancy in breast cancer cell lines. *Nanomedicine (Lond)* **13**, 2597-2609 (2018). https://doi.org:10.2217/nnm-2018-0094

69 Ariotti, N. *et al.* An inverted CAV1 (caveolin 1) topology defines novel autophagy-dependent exosome secretion from prostate cancer cells. *Autophagy* **17**, 2200-2216 (2021). https://doi.org:10.1080/15548627.2020.1820787

70 Abramson, J. *et al.* Accurate structure prediction of biomolecular interactions with AlphaFold 3. *Nature* **630**, 493-500 (2024). https://doi.org:10.1038/s41586-024-07487-w

71 Chang, S. H., Feng, D., Nagy, J. A., Sciuto, T. E., Dvorak, A. M. & Dvorak, H. F. Vascular permeability and pathological angiogenesis in caveolin-1-null mice. *Am J Pathol* **175**, 1768-1776 (2009). https://doi.org:10.2353/ajpath.2009.090171

72 Loo, J. H., Wang, Z. & Chong, R. S. Caveolin-1 in vascular health and glaucoma: A critical vascular regulator and potential therapeutic target. *Front Med (Lausanne)* **10**, 1087123 (2023). https://doi.org:10.3389/fmed.2023.1087123

73 Jiang, Y. *et al.* Critical role of caveolin-1 in ocular neovascularization and multitargeted antiangiogenic effects of cavtratin via JNK. *Proc Natl Acad Sci U S A* **114**, 10737-10742 (2017). https://doi.org:10.1073/pnas.1706394114

74 Gu, X., Fliesler, S. J., Zhao, Y. Y., Stallcup, W. B., Cohen, A. W. & Elliott, M. H. Loss of caveolin-1 causes blood-retinal barrier breakdown, venous enlargement, and mural cell alteration. *Am J Pathol* **184**, 541-555 (2014). https://doi.org:10.1016/j.ajpath.2013.10.022

75 Loo, J. H. *et al.* Loss of Caveolin-1 Impairs Light Flicker-Induced Neurovascular Coupling at the Optic Nerve Head. *Front Neurosci* **15**, 764898 (2021). https://doi.org:10.3389/fnins.2021.764898

76 Orozco, L. D. *et al.* A systems biology approach uncovers novel disease mechanisms in age-related macular degeneration. *Cell Genom* **3**, 100302 (2023). https://doi.org:10.1016/j.xgen.2023.100302

77 Li, Y. *et al.* FRZB: a potential prognostic marker for head and neck squamous cell carcinoma. *Braz J Med Biol Res* **57**, e13368 (2024). https://doi.org:10.1590/1414-431X2024e13368

78 Mandal, D. *et al.* Severe suppression of Frzb/sFRP3 transcription in osteogenic sarcoma. *Gene* **386**, 131-138 (2007). https://doi.org:10.1016/j.gene.2006.08.030

79 Ugolini, F. *et al.* Differential expression assay of chromosome arm 8p genes identifies Frizzled-related (FRP1/FRZB) and Fibroblast Growth Factor Receptor 1 (FGFR1) as candidate breast cancer genes. *Oncogene* **18**, 1903-1910 (1999). https://doi.org:10.1038/sj.onc.1202739

80 An, X. *et al.* WTAP-mediated m(6)A modification of FRZB triggers the inflammatory response via the Wnt signaling pathway in osteoarthritis. *Exp Mol Med* **56**, 156-167 (2024). https://doi.org:10.1038/s12276-023-01135-5

81 Thysen, S., Luyten, F. P. & Lories, R. J. Loss of Frzb and Sfrp1 differentially affects joint homeostasis in instability-induced osteoarthritis. *Osteoarthritis Cartilage* **23**, 275-279 (2015). https://doi.org:10.1016/j.joca.2014.10.010

82 Oh, C. K. *et al.* FRZB as a key molecule in abdominal aortic aneurysm progression affecting vascular integrity. *Biosci Rep* **41** (2021). https://doi.org:10.1042/BSR20203204

83 Bhagat, T. D. *et al.* Epigenetically Aberrant Stroma in MDS Propagates Disease via Wnt/beta-Catenin Activation. *Cancer Res* **77**, 4846-4857 (2017). https://doi.org:10.1158/0008-5472.CAN-17-0282

84 Mocci, G. *et al.* Single-Cell Gene-Regulatory Networks of Advanced Symptomatic Atherosclerosis. *Circ Res* **134**, 1405-1423 (2024). https://doi.org:10.1161/CIRCRESAHA.123.323184

85 Qin, S., Zhang, Z., Li, J. & Zang, L. FRZB knockdown upregulates beta-catenin activity and enhances cell aggressiveness in gastric cancer. *Oncol Rep* **31**, 2351-2357 (2014). https://doi.org:10.3892/or.2014.3109

86 Kim, H. *et al.* Modulating vascular smooth muscle cell phenotype via Wnt-Independent FRZB pathways. *Arch Biochem Biophys* **764**, 110290 (2025). https://doi.org:10.1016/j.abb.2025.110290

87 Guo, Y. *et al.* Frzb, a secreted Wnt antagonist, decreases growth and invasiveness of fibrosarcoma cells associated with inhibition of Met signaling. *Cancer Res* **68**, 3350-3360 (2008). https://doi.org:10.1158/0008-5472.CAN-07-3220

88 Qu, Y. *et al.* Over-expression of FRZB in gastric cancer cell suppresses proliferation and induces differentiation. *J Cancer Res Clin Oncol* **134**, 353-364 (2008). https://doi.org:10.1007/s00432-007-0291-0

89 Zi, X. *et al.* Expression of Frzb/secreted Frizzled-related protein 3, a secreted Wnt antagonist, in human androgen-independent prostate cancer PC-3 cells suppresses tumor growth and cellular invasiveness. *Cancer Res* **65**, 9762-9770 (2005). https://doi.org:10.1158/0008-5472.CAN-05-0103

90 Wu, Z. H., Zhang, Y. J., Yue, J. X. & Zhou, T. Comprehensive Analysis of the Expression and Prognosis for SFRPs in Breast Carcinoma. *Cell Transplant* **29**, 963689720962479 (2020). https://doi.org:10.1177/0963689720962479

91 Qiu, B. *et al.* Apratoxin S4 Inspired by a Marine Natural Product, a New Treatment Option for Ocular Angiogenic Diseases. *Invest Ophthalmol Vis Sci* **60**, 3254-3263 (2019). https://doi.org:10.1167/iovs.19-26936

92 Limb, G. A., Salt, T. E., Munro, P. M., Moss, S. E. & Khaw, P. T. In vitro characterization of a spontaneously immortalized human Muller cell line (MIO-M1). *Invest Ophthalmol Vis Sci* **43**, 864-869 (2002).

93 Mulleder, M., Campbell, K., Matsarskaia, O., Eckerstorfer, F. & Ralser, M. Saccharomyces cerevisiae single-copy plasmids for auxotrophy compensation, multiple marker selection, and for designing metabolically cooperating communities. *F1000Res* **5**, 2351 (2016). https://doi.org:10.12688/f1000research.9606.1

94 Fruttiger, M. Development of the mouse retinal vasculature: angiogenesis versus vasculogenesis. *Invest Ophthalmol Vis Sci* **43**, 522-527 (2002).

95 Drozdetskiy, A., Cole, C., Procter, J. & Barton, G. J. JPred4: a protein secondary structure prediction server. *Nucleic Acids Res* **43**, W389-394 (2015). https://doi.org:10.1093/nar/gkv332

96 Nielsen, H. Predicting Secretory Proteins with SignalP. *Methods Mol Biol* **1611**, 59-73 (2017). https://doi.org:10.1007/978-1-4939-7015-5_6

97 Giulini, M. *et al.* HADDOCK3: A Modular and Versatile Platform for Integrative Modeling of Biomolecular Complexes. *J Chem Inf Model* **65**, 7315-7324 (2025). https://doi.org:10.1021/acs.jcim.5c00969

98 Sastry, G. M., Adzhigirey, M., Day, T., Annabhimoju, R. & Sherman, W. Protein and ligand preparation: parameters, protocols, and influence on virtual screening enrichments. *J Comput Aided Mol Des* **27**, 221-234 (2013). https://doi.org:10.1007/s10822-013-9644-8

Acknowledgments

This work was supported by a Start-Up grant to X. W. at Duke-NUS Medical School; BMRC-SIPRAD grant to X.W, G. C, W.H., and T. W; NMRC – LCG Grant (Grant No. OFLCG23may-0032) for the Translational Asian Age-related macular degeneration Programme (TAAP) to X.W

and G.C, and Support from the InnoHK initiative and the Hong Kong Special Administrative Region Government to L. Z. NTU PPP platform for recombinant protein production.

Author Contributions

X.W. conceived and designed the study. X.W, CJ.C, HT.C, V.A.B, B.Q, R.N.C, S.T.L, C. J. W.S, and A.T performed *in vitro*, *ex vivo*, and *in vivo* angiogenesis assays and analysed the data. L.Z, J.G., A.A-S, and S.K.K. performed proteomics analyses. CJ.C, HT.C, B.Q, R.N.C, and S.T.L. carried out molecular biology and biochemistry studies. R.K.V and H.F modelled the FRZB and CAV-1 interaction. N.C and C.M.C helped with clinical evaluation and patient sample collection. T.Y.W and G.C.C.M provided critical clinical insights and guided the clinical study design. X.W, CJ.C, HT.C, L.Z, J.G., R.K.V, W.S., and H.F drafted the manuscript. D.V, T.Y.W, G.C.C.M, and W.H reviewed, revised, and provided critical comments on the manuscript.

Competing interests

The authors declare no competing interests.

Table 1: Effect of CAV1 mutations on FRZB-CAV1 complex stability.

Condition	$\Delta\Delta G_{MUT}$ (kcal/mol)	$\Delta\Delta G_{WT}$ (kcal/mol)	$\Delta\Delta G$ (kcal/mol)
Y42D	-89.5 ± 28.1	-104.2 ± 29.7	14.7
Y14D	-96.7 ± 29.9		7.5

Figure legends (6)

Figure 1. FRZB expression in normal and diseased eyes. (**A**) Volcano plot of TMT-based quantitative proteomics analysis showing differentially abundant proteins in the vitreous of patients with proliferative diabetic retinopathy (PDR) and control patients with epiretinal membrane (ERM). Proteins showing significant changes in PDR vitreous, including FRZB, are highlighted (left), and a Comparison of the protein abundance ratio of FRZB between control ERM samples (n = 16 patients) and PDR samples (n = 20 patients) (right; $p < 0.0001$). **(B)** Volcano plot of vitreous from PDR (n = 8 patients) and non-PDR retinal detachment (RD) patients (n = 8 patients) using SWATH-MS on a TripleTOF 5600. **(C)** Representative Western blot (top) and densitometry analysis (bottom) of FRZB expression in the vitreous of PDR patients (n = 15 patients) and non-PDR RD controls (n = 6 patients; $p = 0.0034$). **(D)** *Frzb* gene expression in P17 C57BL/6 mouse retinae subjected to normoxia and OIR (n = 7 animals; $p = 0.0018$). **(E)** *Frzb* gene expression in the RPE/choroid complex of C57BL/6 mice at day 14 post-laser injury (n = 4 animals) compared to non-lasered controls (n = 6 animals; $p = 0.0171$). **(F)** *Frzb* gene expression in the retina and RPE/choroidal complex of adult C57BL/6 mice (n = 6 animals; $p < 0.0001$). **(G)** Confocal fluorescence RNAscope analysis assessing *Frzb* RNA expression in FFPE sections of adult mouse eyes, co-stained with the Müller cell marker Glutamine Synthetase (GS). Scale bar, 50µm. **(H)** *FRZB* gene expression in different human ocular cell lines, including human retinal pigment epithelial cells (HRPE; $p < 0.0001$), human retinal endothelial cells (HREC; $p < 0.0001$), human retinal pericytes ($p < 0.0001$), and Muller cells (n = 4 independent experiments). Data are represented as mean ± s.d. Statistical significance was determined by a two-sided Student's t-test or one-way ANOVA. * $p < 0.05$, ** $p < 0.01$, *** $p < 0.001$, **** $p < 0.0001$. Source data are provided as a Source Data file.

Figure 2. Characterization of ocular neovascularization in wild-type and *Frzb*$^{-/-}$ mice. (A-B) Developmental retinal angiogenesis: (A) Representative immunofluorescence images (left) and quantification (right) of retinal vascular radius ($p = 0.001$) and retinal vascular density ($p = 0.0351$) at P4 of wild-type and *Frzb*$^{-/-}$ mice**.** (CD31, green; DAPI, blue; white line: distance between migrating front of retinal vessel and optic nerve head (ONH)**)** (n = 6 animals). **(B)** Representative immunofluorescence images (left) and quantification (right) of retinal vascular density at postnatal stage from P7 (superficial plexus; $p = 0.0001$) to P10 (deep plexus; $p = 0.0003$; CD31, green) (n = 6 animals). **(C)** Oxygen-induced retinopathy (OIR) model: Representative images of immunofluorescence staining of retinal flatmounts stained with vascular marker CD31 (green, left) and quantitative analysis of the total area of avascularisation region and neovascularization tuft (right; $p = 0.0076$) in P17 OIR retinas (n = 5 wild-type and *Frzb*$^{-/-}$ animals for quantifying avascular area; n = 8 wild-type and n = 7 *Frzb*$^{-/-}$ animals for quantifying tuft area). The avascular region is highlighted in red. **(D-E)** Laser-induced choroidal neovascularization model: **(D)** Representative images (left) and quantification (right) of fundus fluorescein angiography (FFA) on post-laser day 14 in wild-type and *Frzb*$^{-/-}$ mice subjected to laser-induced choroidal neovascularization (CNV) (n = 5 animals; $p = 0.0012$). **(E)** Representative immunofluorescence images of RPE flatmounts stained with CD31 (green, left) and quantitative analysis of CD31-positive CNV lesion area (right) on post-laser day 14 (n = 9 wild-type and n = 6 *Frzb*$^{-/-}$ mice; $p = 0.0181$). Data are presented as mean ± s.d. Statistical significance was determined by a two-sided Student's t-test. * $p < 0.05$, ** $p < 0.01$, *** $p < 0.001$, **** $p < 0.0001$. Source data are provided as a Source Data file.

Figure 3. **FRZB and its NTR domain inhibit endothelial cell activation and angiogenesis *in vitro* and *ex vivo*. (A)** Alamar blue proliferation assay of HRECs following 24-hour treatment with vehicle, Fc-CRD, Fc-NTR ($p < 0.0001$), or Fc-FRZB ($p < 0.0001$) (n = 3 independent experiments). **(B)** Representative images (left) and quantification (right) of HREC tube formation in Matrigel following 16-hour treatment (n = 3 independent experiments). Total tube length: Vehicle vs. Fc-NTR, $p = 0.0302$; Vehicle vs. Fc-FRZB, $p = 0.0239$. Number of junctions: Vehicle vs. Fc-NTR, $p = 0.0125$; Vehicle vs. Fc-FRZB, $p = 0.0064$). Scale bar, 200µm. **(C)** Representative images (left) and quantification (right) of DAPI-labelled HRECs migrated across Transwell after 4-hour treatment with vehicle, Fc-CRD, Fc-NTR ($p < 0.0001$), or Fc-FRZB ($p < 0.0001$; n = 7 independent experiments). Scale bar, 150µm. **(D)** Representative images (left) and quantification (right) of DAPI-labelled THP1 cells adhered to the HREC monolayer following 2-hour treatment with vehicle, Fc-CRD, Fc-NTR ($p = 0.0049$), or Fc-FRZB ($p < 0.0001$; n = 5 independent experiments). Scale bar, 50µm. **(E)** Representative images (left) and quantification (right) of vessel outgrowth from C57BL/6 mouse choroid explants treated with vehicle (n = 8 explants), Fc-NTR ($p = 0.0068$; n = 8 explants), and Fc-FRZB ($p = 0.0428$; n = 7 explants). Scale bar, 500µm. **(F)** Representative images (left) and quantification (right) of CD31-positive sprouts from C57BL/6 mouse aortic rings treated with vehicle (n = 18 explants), 500 nM Fc-NTR ($p = 0.0204$; n = 9 explants), and Fc-FRZB ($p < 0.0001$; n = 9 explants). Scale bar, 400µm. **(G)** Representative images (left) and quantification (right) of CD31-positive vessels from C57BL/6 mouse metatarsal explants treated with vehicle (n = 8 explants), Fc-NTR ($p = 0.0141$; n = 7 explants), and Fc-FRZB ($p = 0.009$; n = 7 explants). Scale bar, 200µm. Data are represented as means ± s.d. Statistical significance was determined by one-way ANOVA * $p < 0.05$, ** $p < 0.01$, *** $p < 0.001$, and

**** $p < 0.0001$. 500µM recombinant proteins were used in all assays. Source data are provided as a Source Data file.

Figure 4. **Fc-FRZB and Fc-NTR prevent and reverse ocular angiogenesis *in vivo*. (A)** Schematic of prevention laser-induced CNV model. **(B)** FFA images (left) and quantification (right) of C57BL/6 mice treated with vehicle (n = 24), Aflibercept (n = 24), Fc-NTR (n = 23), Fc-FRZB (n = 24), Fc-NTR/Aflibercept (n = 22), and Fc-FRZB/Aflibercept (n = 21) 14 days after laser. All treatments reduced leakage vs Vehicle ($p < 0.0001$). Aflibercept vs. Fc-NTR, $p = 0.0144$; Aflibercept vs. Fc-NTR/Aflibercept, $p < 0.0001$; Aflibercept vs. Fc-FRZB/Aflibercept, $p = 0.001$. Scale bar: 500µm. **(C)** CD31 immunofluorescence images (left) and quantification (right) of CNV lesions in C57BL/6 mice treated with vehicle (n = 14), Aflibercept (n = 14), Fc-NTR (n = 9), Fc-FRZB (n = 8), Fc-NTR/Aflibercept (n = 14), and Fc-FRZB/Aflibercept (n = 14) 14 days after laser (Vehicle vs. Aflibercept, $p = 0.0451$; Vehicle vs. Fc-NTR, $p = 0.0006$; Vehicle vs. Fc-FRZB, $p = 0.0002$; Vehicle vs. Fc-NTR/Aflibercept, $p = 0.0004$; Vehicle vs. Fc-FRZB/Aflibercept, $p = 0.0044$). Scale bar: 100µm. **(D)** Schematic of regression laser-induced CNV model. **(E)** FFA images (left) and quantification (right) of C57BL/6 mice treated with vehicle, Aflibercept, Fc-NTR, and Fc-FRZB (n = 24) day 17 after laser. All treatments reduced leakage vs Vehicle ($p < 0.0001$). Scale bar: 500µm. **(F)** CD31 immunofluorescence images (left) and quantification (right) of CNV lesions in C57BL/6 mice treated with vehicle (n = 16), Aflibercept (n = 18), Fc-NTR (n = 8), and Fc-FRZB (n = 21) day 17 after laser (vs Vehicle: Aflibercept, $p = 0.0102$; Fc-NTR, $p = 0.0244$; Fc-FRZB, $p = 0.0008$). Scale bar: 100µm. **(G)** CD31 immunofluorescence images (left) and quantification (right) of neovascular tufts in P17 OIR mice (both treatments reduce neovascularization vs. Vehicle ($p < 0.0001$; n = 10). Scale bar: 500µm, 200µm. **(H)** FFA images

of persistent retinal neovascularization (PRNV) rabbits following vehicle or Fc-NTR treatment. Scale bar: 0.1mm. n represents animal numbers. Data are presented as mean ± s.d. Statistical significance was determined by one-way ANOVA. * p <0.05, ** p <0.01, *** p < 0.001, **** p < 0.0001. Source data are provided as a Source Data file. The Schematic illustration of the experimental design was generated using PowerPoint.

Figure 5. **FRZB controls angiogenesis *via* Cav-1-mediated TGFβ receptor dynamics. (A)** Western blot of pLRP6, β-Catenin, and GAPDH in HRECs treated with Wnt1 and/or Fc-NTR, for 30 minutes. **(B)** Western blots of pVEGFR2, VEGFR2, and GAPDH in HRECs treated with vehicle, VEGFa, VEGFa/Aflibercept, or VEGFa/Fc-FRZB. **(C)** Western blots of pSMAD1/5, SMAD1/5, pSMAD3, SMAD3, ALK5, ALK1, and GAPDH in control or Fc-FRZB-treated HRECs. **(D)** Western blots of pSMAD3, SMAD3, and GAPDH in HRECs treated with SB431542 and/or Fc-FRZB for 1 hour. **(E)** Hierarchical clustering revealed that the level of QVY42DAHTK originated from CAV1 was reduced in Fc-FRZB-treated HRECs as compared to control. **(F)** Images (left) and quantification (right) of CAV1Y42D or CAV1Y14D overexpressing HREC tube formation in Matrigel in the presence or absence of Fc-FRZB (n = 6 independent experiments; total tube length: pcDNA3.1 vs. Fc-FRZB, p = 0.0002; pcDNA3.1 vs. Y14D + Fc-FRZB, p = 0.0027; number of junctions: pcDNA3.1 vs. Fc-FRZB, p = 0.0005; pcDNA3.1 vs. Y14D + Fc-FRZB, p = 0.0003; pcDNA3.1 vs. Y14D, p = 0.053). Scale bar, 200μm. **(G)** Images (left) and quantification (right) of DAPI-positive CAV1Y42D overexpressing HRECs migrated across the Transwell in the presence or absence of Fc-FRZB (n = 4 independent experiments; pcDNA3.1 vs. Fc-FRZB, p = 0.002; Fc-FRZB vs. CAV1 Y42D, p = 0.0003; Fc-FRZB vs. CAV1 Y42D + Fc-FRZB, p = 0.0184). Scale bar, 150μm. **(H)** Western blot of pSMAD1/5, SMAD1/5, pSMAD3,

SMAD3, ALK5, ALK1, and GAPDH in WT and CAV1Y42D overexpressing HRECs in the presence or absence of FRZB. **(I)** Co-immunoprecipitation (IP) assay evaluating the interaction between FRZB and CAV1 in HEK293 Cell lysate and supernatant. **(J)** Modelled FRZB-CAV1 complex: CRD (pink), NTR (grey), CAV1 (green), the hydrogen bond between Tyr42 of CAV1 and the β-sheet within the NTR domain of FRZB (orange). Each experiment was independently replicated at least three times, with reproducible and consistent results observed. Data are presented as mean ± s.d. Statistical significance was determined by one-way ANOVA. * $p < 0.05$, ** $p < 0.01$, *** $p < 0.001$. Source data are provided as a Source Data file.

Figure 6. **Working Model of FRZB-Regulated TGFβ Signalling in Retinal Endothelial Cells.** Caveolin-1 (Cav1) decorates the outer surface of exosomes, enabling direct interaction with secreted FRZB. This interaction inhibits Cav1 phosphorylation at a previously uncharacterised Tyr42 site. Re-incorporation of dephosphorylated Cav1-enriched exosomes into the plasma membrane impairs caveolae-dependent endocytosis of the TGF-β receptor complex. Consequently, increased levels of ALK5 are retained at the cell surface, leading to enhanced TGF-β binding and activation, elevated phosphorylation of the downstream signalling transducers Smad2/3, and ultimately suppression of angiogenesis. The figure was created in BioRender. Chia, R. N. (2026) https://BioRender.com/r0oy1eh.

Editorial Summary:
Pathological neovascularization is a leading cause of vision loss. In this study, the authors identify FRZB and its NTR domain as suppressors of ocular angiogenesis. FRZB prevents CAV1 phosphorylation at Tyr42 which enhances downstream TGFβ signaling via ALK5 retention.
Peer review information: *Nature Communications* thanks Alexander Ljubimov and the other, anonymous, reviewer(s) for their contribution to the peer review of this work. A peer review file is available.

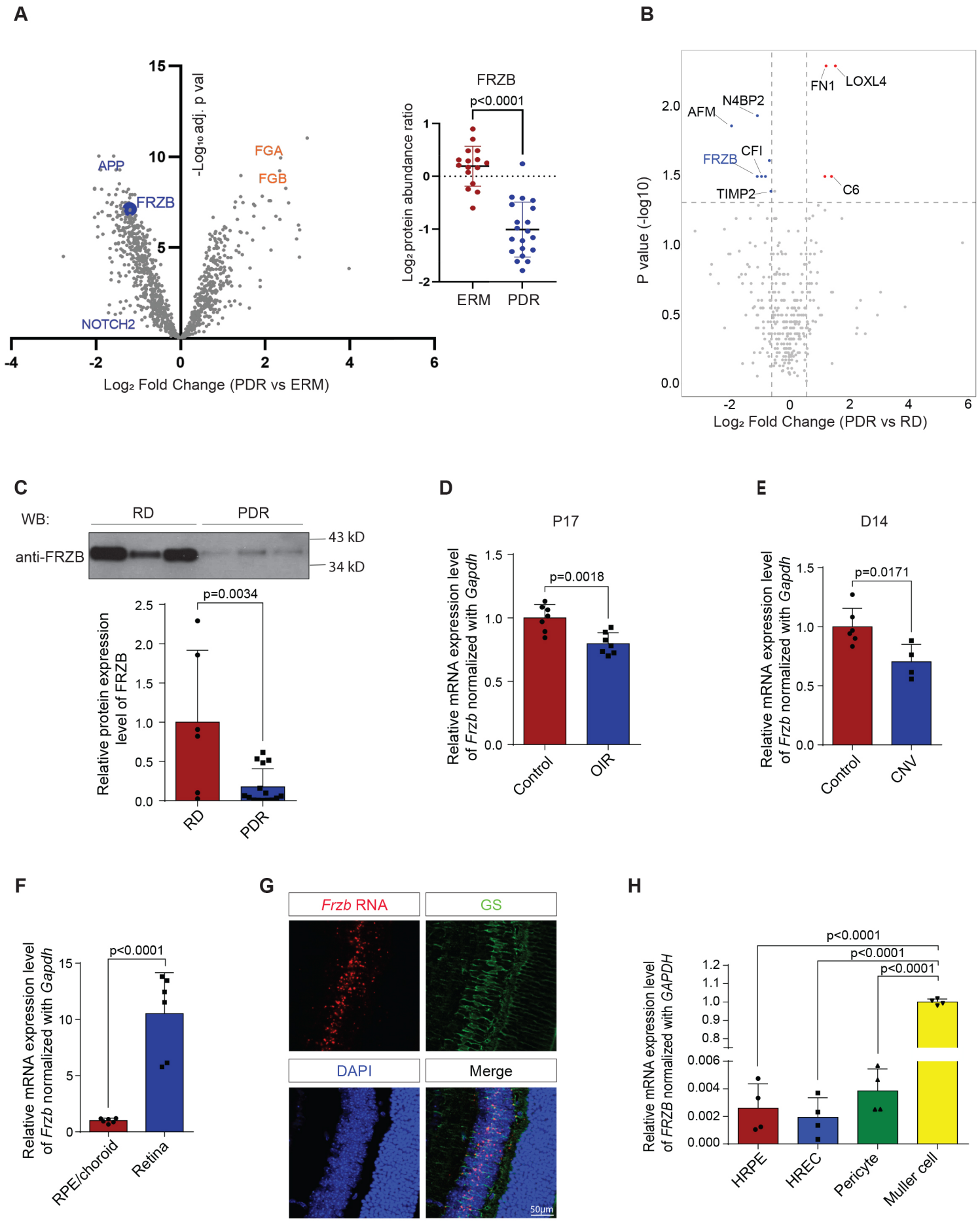
A
-Log10 adj. p val
APP
FRZB
NOTCH2
FGA
FGB
Log2 Fold Change (PDR vs ERM)
FRZB
p<0.0001
Log2 protein abundance ratio
ERM
PDR
B
FN1
LOXL4
N4BP2
AFM
FRZB
CFI
TIMP2
C6
P value (-log10)
Log2 Fold Change (PDR vs RD)
C
WB:
RD
PDR
anti-FRZB
43 kD
34 kD
p=0.0034
Relative protein expression level of FRZB
D
P17
p=0.0018
Relative mRNA expression level of Frzb normalized with Gapdh
Control
OIR
E
D14
p=0.0171
Relative mRNA expression level of Frzb normalized with Gapdh
Control
CNV
F
p<0.0001
Relative mRNA expression level of Frzb normalized with Gapdh
RPE/choroid
Retina
G
Frzb RNA
GS
DAPI
Merge
50μm
H
p<0.0001
p<0.0001
p<0.0001
Relative mRNA expression level of FRZB normalized with GAPDH
HRPE
HREC
Pericyte
Muller cell

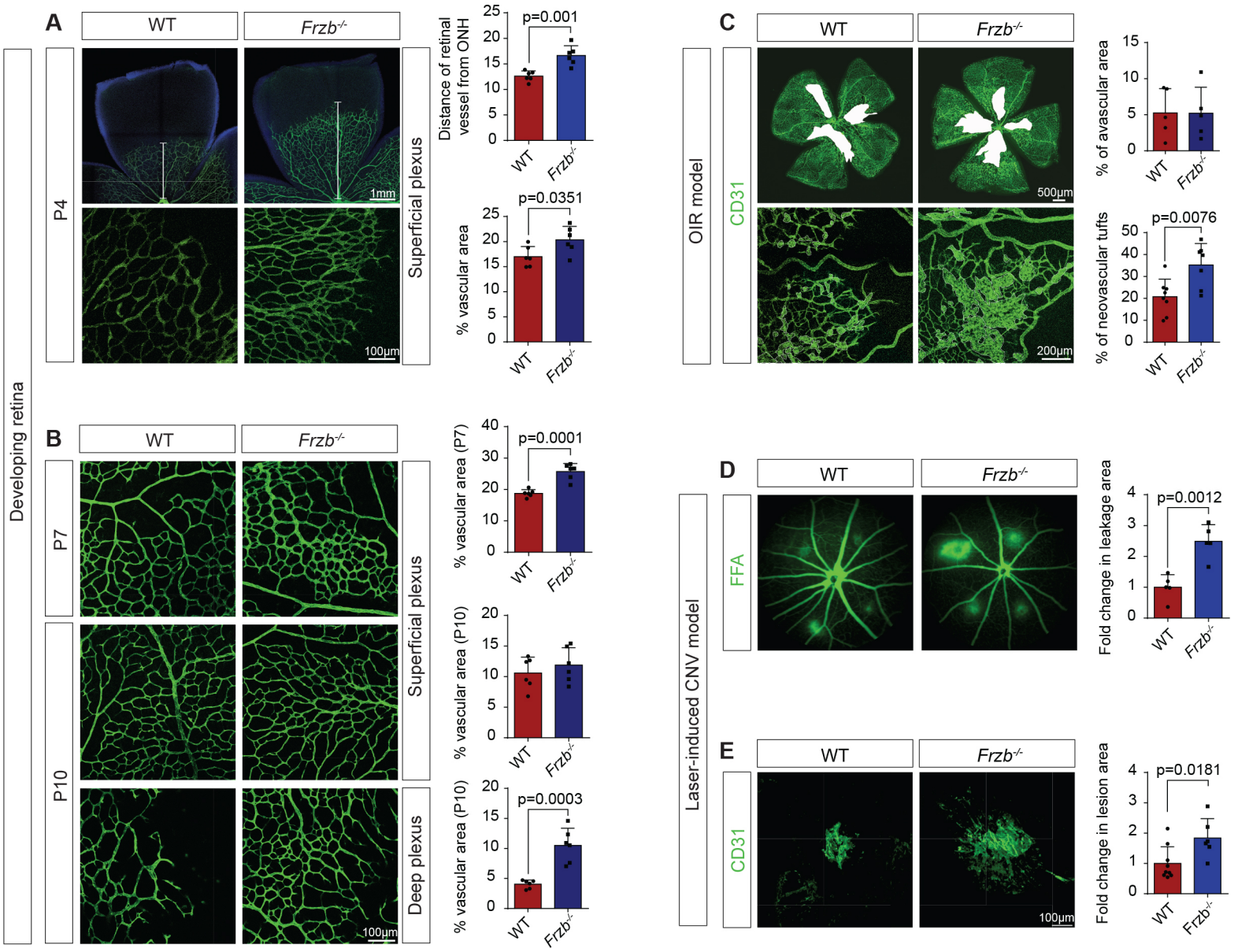
A
WT
Frzb-/-
P4
Superficial plexus
1mm
100µm
Distance of retinal vessel from ONH
p=0.001
% vascular area
p=0.0351
B
P7
P10
Superficial plexus
Deep plexus
% vascular area (P7)
p=0.0001
% vascular area (P10)
% vascular area (P10)
p=0.0003
C
OIR model
CD31
500µm
200µm
% of avascular area
% of neovascular tufts
p=0.0076
D
Laser-induced CNV model
FFA
Fold change in leakage area
p=0.0012
E
CD31
100µm
Fold change in lesion area
p=0.0181
Developing retina

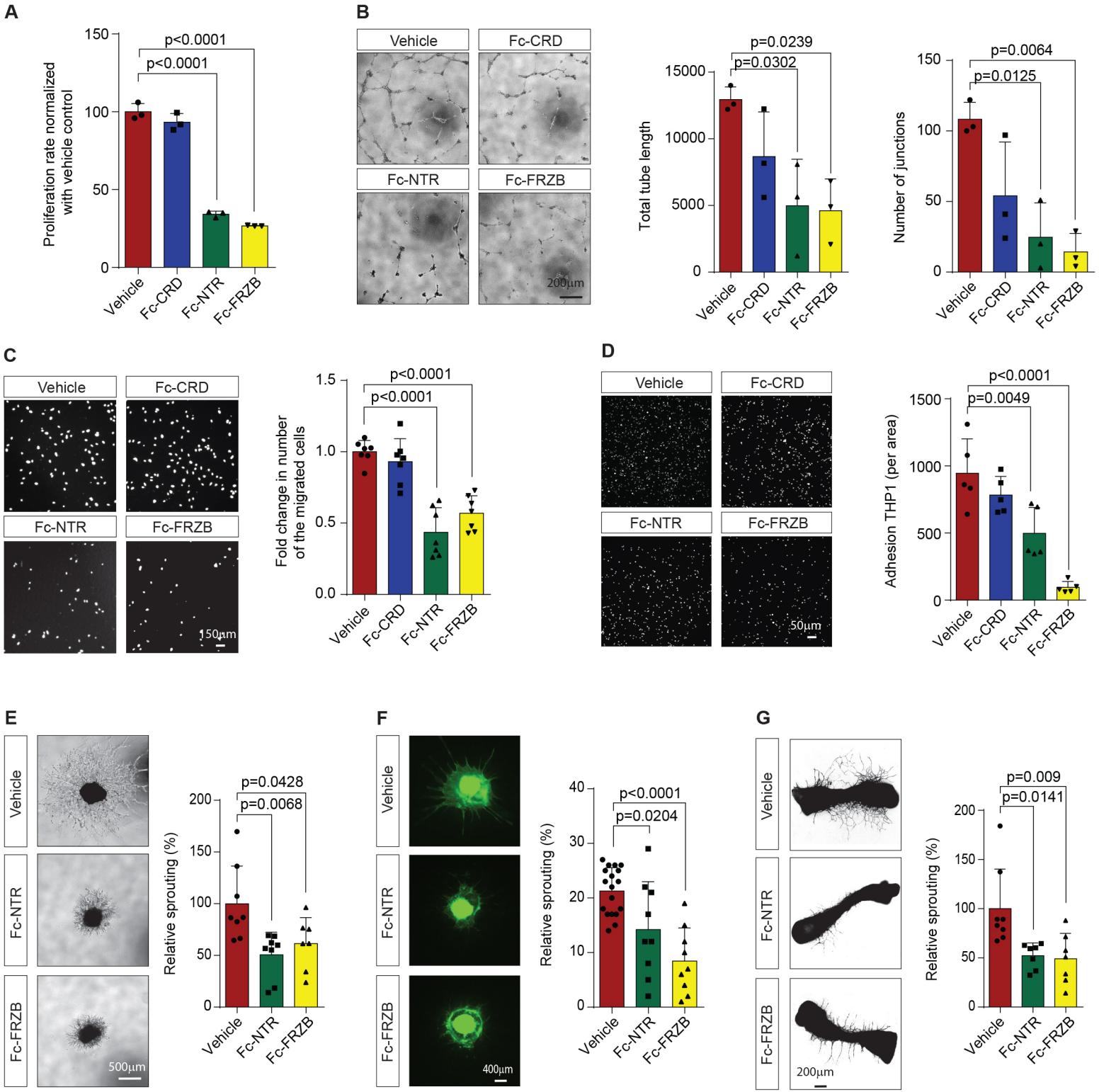
A
Proliferation rate normalized with vehicle control
150
100
50
0
p<0.0001
p<0.0001
Vehicle
Fc-CRD
Fc-NTR
Fc-FRZB
B
Vehicle
Fc-CRD
Fc-NTR
Fc-FRZB
200µm
Total tube length
15000
10000
5000
0
p=0.0239
p=0.0302
Number of junctions
150
100
50
0
p=0.0064
p=0.0125
C
Vehicle
Fc-CRD
Fc-NTR
Fc-FRZB
150µm
Fold change in number of the migrated cells
1.5
1.0
0.5
0.0
p<0.0001
p<0.0001
D
Vehicle
Fc-CRD
Fc-NTR
Fc-FRZB
50µm
Adhesion THP1 (per area)
1500
1000
500
0
p<0.0001
p=0.0049
E
Vehicle
Fc-NTR
Fc-FRZB
500µm
Relative sprouting (%)
200
150
100
50
0
p=0.0428
p=0.0068
F
Vehicle
Fc-NTR
Fc-FRZB
400µm
Relative sprouting (%)
40
30
20
10
0
p<0.0001
p=0.0204
G
Vehicle
Fc-NTR
Fc-FRZB
200µm
Relative sprouting (%)
200
150
100
50
0
p=0.009
p=0.0141

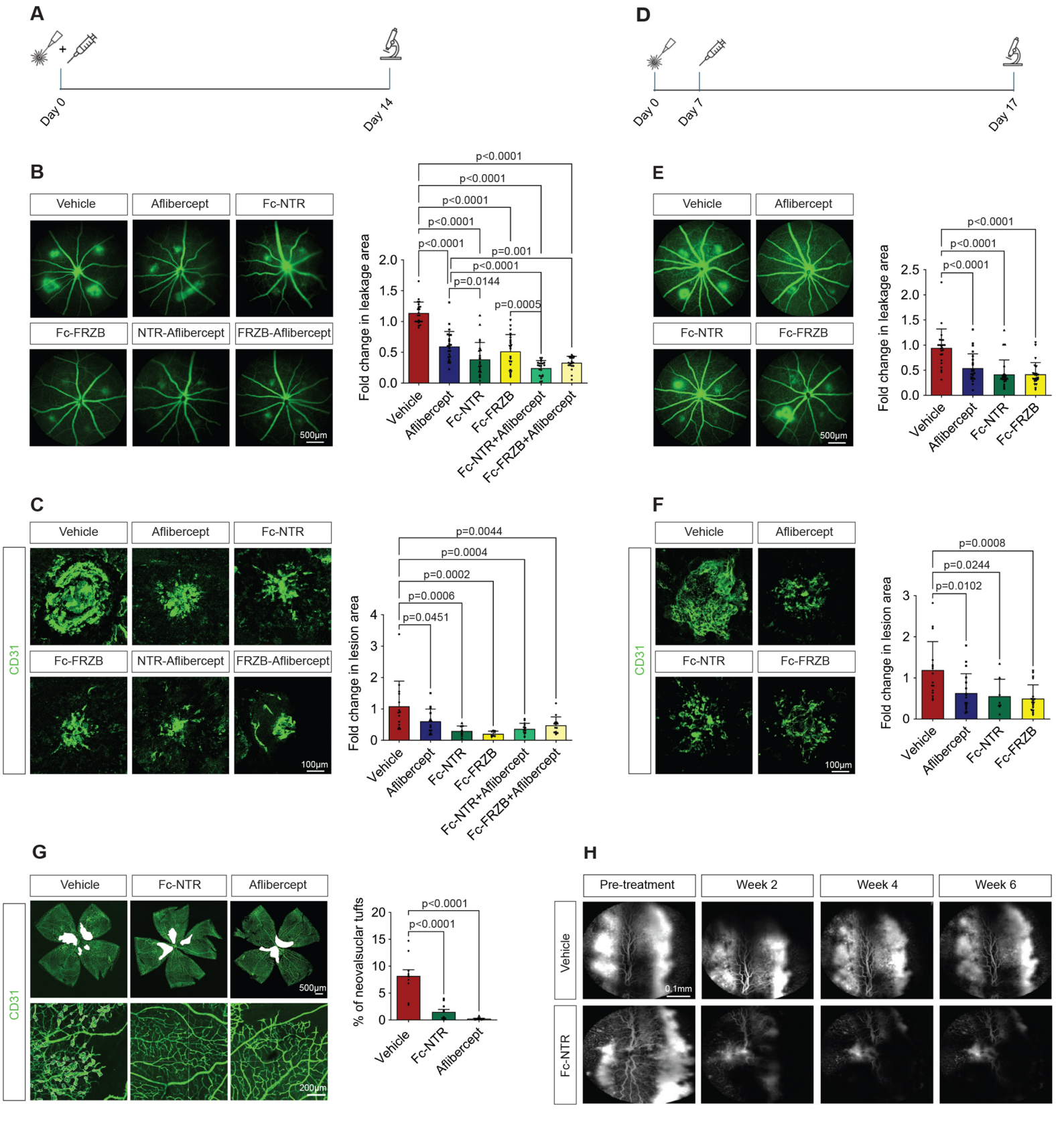
A
Day 0
Day 14
D
Day 0
Day 7
Day 17
B
Vehicle
Aflibercept
Fc-NTR
Fc-FRZB
NTR-Aflibercept
FRZB-Aflibercept
500µm
Fold change in leakage area
p<0.0001
p<0.0001
p<0.0001
p<0.0001
p<0.0001
p=0.001
p<0.0001
p=0.0144
p=0.0005
Vehicle
Aflibercept
Fc-NTR
Fc-FRZB
Fc-NTR+Aflibercept
Fc-FRZB+Aflibercept
E
Vehicle
Aflibercept
Fc-NTR
Fc-FRZB
500µm
Fold change in leakage area
p<0.0001
p<0.0001
p<0.0001
Vehicle
Aflibercept
Fc-NTR
Fc-FRZB
C
CD31
Vehicle
Aflibercept
Fc-NTR
Fc-FRZB
NTR-Aflibercept
FRZB-Aflibercept
100µm
Fold change in lesion area
p=0.0044
p=0.0004
p=0.0002
p=0.0006
p=0.0451
Vehicle
Aflibercept
Fc-NTR
Fc-FRZB
Fc-NTR+Aflibercept
Fc-FRZB+Aflibercept
F
CD31
Vehicle
Aflibercept
Fc-NTR
Fc-FRZB
100µm
Fold change in lesion area
p=0.0008
p=0.0244
p=0.0102
Vehicle
Aflibercept
Fc-NTR
Fc-FRZB
G
CD31
Vehicle
Fc-NTR
Aflibercept
500µm
200µm
% of neovalsuclar tufts
p<0.0001
p<0.0001
Vehicle
Fc-NTR
Aflibercept
H
Pre-treatment
Week 2
Week 4
Week 6
Vehicle
Fc-NTR
0.1mm

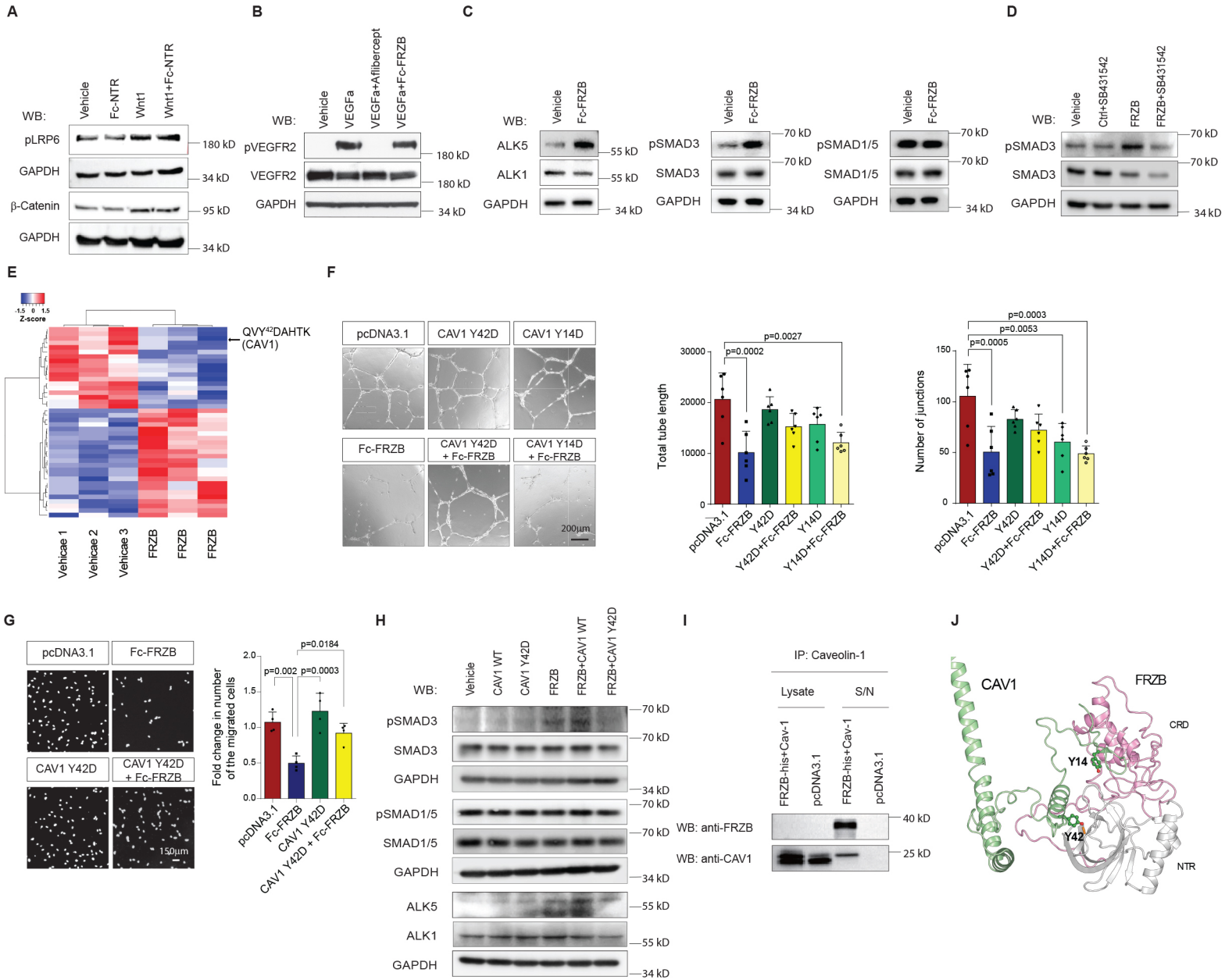
A
WB:
Vehicle
Fc-NTR
Wnt1
Wnt1+Fc-NTR
pLRP6
180 kD
GAPDH
34 kD
β-Catenin
95 kD
GAPDH
34 kD
B
WB:
Vehicle
VEGFa
VEGFa+Aflibercept
VEGFa+Fc-FRZB
pVEGFR2
180 kD
VEGFR2
180 kD
GAPDH
34 kD
C
WB:
Vehicle
Fc-FRZB
ALK5
55 kD
ALK1
55 kD
GAPDH
34 kD
pSMAD3
70 kD
SMAD3
70 kD
GAPDH
34 kD
pSMAD1/5
70 kD
SMAD1/5
70 kD
GAPDH
34 kD
D
WB:
Vehicle
Ctrl+SB431542
FRZB
FRZB+SB431542
pSMAD3
70 kD
SMAD3
70 kD
GAPDH
34 kD
E
Z-score
-1.5 0 1.5
QVY42DAHTK
(CAV1)
Vehicae 1
Vehicae 2
Vehicae 3
FRZB
FRZB
FRZB
F
pcDNA3.1
CAV1 Y42D
CAV1 Y14D
Fc-FRZB
CAV1 Y42D
+ Fc-FRZB
CAV1 Y14D
+ Fc-FRZB
200µm
Total tube length
p=0.0002
p=0.0027
pcDNA3.1
Fc-FRZB
Y42D
Y42D+Fc-FRZB
Y14D
Y14D+Fc-FRZB
Number of junctions
p=0.0005
p=0.0053
p=0.0003
G
pcDNA3.1
Fc-FRZB
CAV1 Y42D
CAV1 Y42D
+ Fc-FRZB
150µm
Fold change in number
of the migrated cells
p=0.002
p=0.0003
p=0.0184
pcDNA3.1
Fc-FRZB
CAV1 Y42D
CAV1 Y42D + Fc-FRZB
H
WB:
Vehicle
CAV1 WT
CAV1 Y42D
FRZB
FRZB+CAV1 WT
FRZB+CAV1 Y42D
pSMAD3
70 kD
SMAD3
70 kD
GAPDH
34 kD
pSMAD1/5
70 kD
SMAD1/5
70 kD
GAPDH
34 kD
ALK5
55 kD
ALK1
55 kD
GAPDH
34 kD
I
IP: Caveolin-1
Lysate
S/N
FRZB-his+Cav-1
pcDNA3.1
FRZB-his+Cav-1
pcDNA3.1
WB: anti-FRZB
40 kD
WB: anti-CAV1
25 kD
J
CAV1
FRZB
CRD
Y14
Y42
NTR

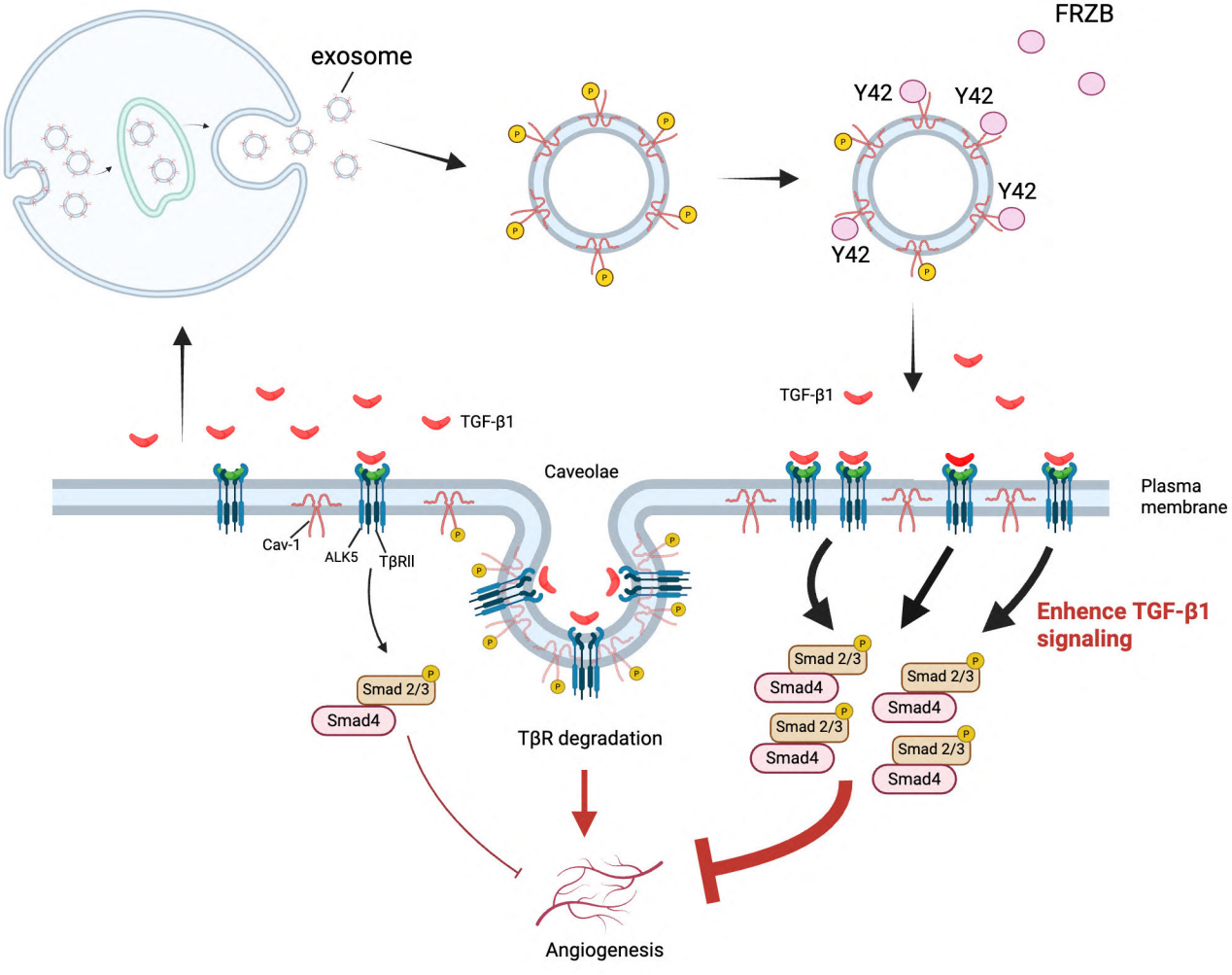
exosome
FRZB
Y42
Y42
Y42
Y42
TGF-β1
TGF-β1
Caveolae
Plasma membrane
Cav-1
ALK5
TβRII
Smad 2/3
Smad4
TβR degradation
Smad 2/3
Smad4
Smad 2/3
Smad4
Smad 2/3
Smad4
Enhence TGF-β1 signaling
Angiogenesis